Aus dem Institut für Computerunterstütze Klinische Medizin
der Medizinischen Fakultät Mannheim
(Komm. Direktor: Prof. Dr. Ing. Frank G. Zöllner)

Accelerating B_1 Magnitude and Phase Acquisition for Rapid Conductivity Mapping in MRI

Inauguraldissertation
zur Erlangung des Doctor scientiarum humanarum (Dr. sc. hum.)
der
Medizinischen Fakultät Mannheim
der Ruprecht-Karls Universität
zu
Heidelberg

vorgelegt von
Safa Özdemir

aus
Malatya, Türkei

2023

Dekan: Prof. Dr. med. Sergij Goerdt
Referent: Prof. Dr. Ing. Frank G. Zöllner

Accelerating B_1 Magnitude and Phase Acquisition for Rapid Conductivity Mapping in MRI

Conductivity emerges as a valuable tool for both diagnostic and therapeutic applications. Utilizing complex B_1 fields in MRI, conductivity calculations can be achieved non-invasively and without the need for additional hardware. However, existing methods face challenges in translating this capability into clinical settings due to slow acquisition times, with initial experiments taking over half an hour and even exceeding 8 hours with multi-transmit schemes. This work addresses these limitations by introducing new acquisition schemes for both B_1 magnitude and phase. Specifically, for B_1 magnitude, an undersampling approach coupled with Total Generalized Variation regularization was implemented, demonstrating an impressive 85-fold acceleration in phantom experiments without compromising image quality. For B_1 phase, variable density spiral acquisitions were employed and combined with the SPIRiT parallel imaging technique for image quality enhancement. Phantom and in vivo experiments illustrated close agreement between calculated and expected conductivity values. This acquisition scheme enables the acquisition of a single slice with multiple averages within a second, while achieving whole brain coverage in just a minute. In conclusion, this work substantially reduces overall acquisition time, making it possible to map B_1 magnitude and phase for the whole-brain in less than 2 minutes, thereby enhancing the practicality of MRI-based conductivity imaging in clinical applications.

Beschleunigung der B_1-Magnituden- und Phasenerfassung für die schnelle Leitfähigkeitskartierung in der MRT

Die Leitfähigkeit erweist sich als wertvolles Instrument für diagnostische und therapeutische Anwendungen. Durch die Nutzung komplexer B_1-Felder in der MRT können Leitfähigkeitsberechnungen nicht-invasiv und ohne zusätzliche Hardware durchgeführt werden. Bestehende Methoden stehen jedoch vor der Herausforderung, diese Fähigkeit in klinische Umgebungen zu übertragen, da die Akquisitionszeiten zu lang sind, wobei erste Experimente mehr als eine halbe Stunde und sogar mehr als 8 Stunden bei Mehrfachübertragungsschemata dauerten. Diese Arbeit geht auf diese Einschränkungen ein, indem sie neue Erfassungsschemata für B_1-Magnitude und -Phase einführt. Insbesondere für die B_1-Magnitude wurde ein Ansatz zur Unterabtastung in Verbindung mit der Total Generalized Variation Regularization implementiert, der eine beeindruckende 85-fache Beschleunigung in Phantomexperimenten ohne Beeinträchtigung der Bildqualität zeigt. Für die B_1-Phase wurden Spiralaufnahmen mit variabler Dichte verwendet und mit der parallelen SPIRiT-Bildgebungstechnik zur Verbesserung der Bildqualität kombiniert. Phantom- und In-vivo-Experimente zeigten eine gute Übereinstimmung zwischen berechneten und erwarteten Leitfähigkeitswerten. Dieses Aufnahmeschema ermöglicht die Aufnahme einer einzigen Schicht mit mehreren Durchschnittswerten innerhalb einer Sekunde, wobei das gesamte Gehirn in nur einer Minute erfasst werden kann. Zusammenfassend lässt sich sagen, dass diese Arbeit die Gesamterfassungszeit erheblich verkürzt und es möglich macht, die B_1-Magnitude und -Phase für das gesamte Gehirn in weniger als 2 Minuten abzubilden, wodurch die praktische Anwendbarkeit der MRT-basierten Leitfähigkeitsbildgebung in klinischen Anwendungen verbessert wird.

Contents

1 Introduction **1**

1.1 Background Information 1
1.2 Motivation 2
1.3 Outline 3

2 Theoretical Background **5**

2.1 Nuclear Magnetic Resonance 5
2.1.1 Nuclear Spin 5
2.1.2 Macroscopic Magnetization 6
2.1.3 Faraday's Law of Induction 8
2.1.4 Precession 9
2.1.5 RF Excitation 10
2.1.6 Relaxation 11
2.1.7 Bloch Equations 14
2.2 Magnetic Resonance Imaging 14
2.2.1 Gradient Fields 14
2.2.2 Signal Equation 15
2.2.3 Signal Localization 16
2.3 Standard MRI Pulse Sequences 21
2.3.1 Gradient Echo 21
2.3.2 Spin Echo 22
2.3.3 Balanced Steady-State Free Precession 23
2.4 Accelerated Data Acquisition 25
2.4.1 Parallel Imaging 25
2.4.2 Sampling Techniques 27
2.5 Conductivity in MRI 29
2.5.1 Electrical Properties of Tissues 29
2.5.2 Electrical Properties Imaging 30
2.5.3 Conductivity Reconstruction Techniques 31
2.5.4 B_1 Magnitude Acquisition 34
2.5.5 B_1 Phase Acquisition 36

3 Methods **39**
3.1 Accelerating B_1 Magnitude . . . 39
3.1.1 Data Acquisition . . . 39
3.1.2 Data Processing . . . 41
3.2 Accelerating B_1 Phase . . . 43
3.2.1 Data Acquisition . . . 43
3.2.2 Data Processing . . . 46

4 Results **47**
4.1 Accelerating B_1 Magnitude . . . 47
4.2 Accelerating B_1 Phase . . . 50
4.2.1 Phantom Measurements . . . 50
4.2.2 In Vivo Brain Measurements . . . 54

5 Discussion **57**
5.1 Accelerating B_1 Magnitude . . . 57
5.2 Accelerating B_1 Phase . . . 58

6 Conclusion and Outlook **63**

List of Figures **65**

List of Tables **67**

Curriculum Vitae **69**

List of Publications **71**

Bibliography **75**

Declaration **85**

1 Introduction

1.1 Background Information

Conductivity, the intrinsic property of tissues and organs to conduct electrical currents, has emerged as a valuable diagnostic tool in medical imaging and healthcare. Tissue conductivity is intimately linked to its physiological and pathological state [1]–[3]. Deviations in tissue conductivity can be indicative of various health conditions, including tumors [4], inflammation [5], and edema [5], [6]. Moreover, conductivity plays a pivotal role in various therapeutic applications, such as transcranial magnetic stimulation (TMS) [7], transcranial direct current stimulation [8], radiofrequency ablation (RFA) [9], and calculating specific absorption rate (SAR) [10]. Therefore, the utilization of conductivity as a diagnostic and therapeutic tool holds great promise for early disease detection, individualized treatment planning, and monitoring treatment response, ultimately enhancing the precision and effectiveness of healthcare interventions.

Several techniques have been developed to measure tissue conductivity, each with its own advantages and limitations. Traditionally, tissue biopsies have been employed to directly assess electrical properties [11], but this invasive approach is often limited in its ability to provide a comprehensive spatial evaluation, and, being invasive, carries risks of excessive bleeding and infection. There are also non-invasive imaging methods available to measure conductivity. Electrical Impedance Tomography (EIT) offers a method to monitor conductivity changes within the body by measuring impedance variations at the body's surface using surface electrodes [12]. Magnetic Impedance Tomography (MIT) is another technique that combines magnetic fields with impedance measurements [13]. MIT employs external coils to induce a current within the body and measures impedance changes. Nevertheless, these approaches produce images with limited spatial detail within internal areas due to the relatively low sensitivity of surface potential measurements to changes in electrical properties occurring at a distance from the surface. To overcome this issue, Magnetic Resonance Electical Impedance Tomography (MREIT) was introduced [14]–[17]. This technique integrates magnetic resonance imaging (MRI) with electrical impedance measurements to produce high-resolution conductivity maps.

However, the challenge in MREIT remains achieving adequate resolution while lowering the externally applied current to ensure safety within established limits.

Magnetic Resonance Electrical Properties Tomography (MREPT) aims to create images of electrical properties using the magnetic fields produced when currents are induced at the Larmor frequency, which is the characteristic frequency of the MRI system. Therefore, this technique is non-invasive and does not require any additional hardware. While the idea for MREPT was first proposed by Haacke in 1991 [18], it was first put into practice over a decade later by Wen [19] and systematic research on MREPT only started by Katscher in 2009 [10].

Traditionally, MREPT requires complex B_1 information [10], including both magnitude and phase, to accurately estimate conductivity. However, recent advancements in the field have led to the introduction of phase-based MREPT techniques [20], [21]. These innovative methods are designed to eliminate the need for magnitude information by leveraging a set of carefully considered assumptions. By focusing solely on phase data, phase-based MREPT approaches offer the potential for streamlined and more efficient imaging processes, reducing the complexity of data acquisition and analysis while still providing valuable insights into tissue electrical properties.

MREPT plays a crucial role in healthcare by aiding in the diagnosis and detection of various medical conditions. It offers valuable insights into glioma [22], assisting in precise tumor characterization. MREPT also helps differentiate between hemorrhagic and ischemic strokes [23], facilitating timely interventions. Furthermore, it contributes to the early detection of breast cancer [24] by providing detailed information on tissue electrical properties. This diverse range of applications underscores MREPT's importance in improving diagnostic accuracy and patient outcomes across multiple medical conditions.

1.2 Motivation

Standard MREPT techniques rely on the acquisition of both B_1 phase and magnitude information. Even in phase-based MREPT techniques, B_1 phase data remain essential. The speed at which these data are obtained is crucial, especially in the context of time-sensitive clinical applications. Consequently, the search for optimized pulse sequences capable of efficiently capturing both B_1 phase and magnitude information is a key consideration, ensuring the practicality and effectiveness of MREPT in clinical settings, where prompt and accurate diagnosis is essential.

In the context of obtaining B_1 phase data for MREPT, various pulse sequences are available, each with its own set of advantages and drawbacks. Gradient echo-based sequences [25], for instance, are susceptible to off-resonance artifacts that can affect data accuracy. Ultra-short echo time (UTE) [26] or zero echo time (ZTE) [27] sequences may produce streaking artifacts, which can be further amplified during the Laplacian operation in conductivity calculations. Consequently, in the field of MREPT, spin-echo-based [20] and balanced steady-state free precession (bSSFP) [28] sequences have gained prominence. Spin-echo acquisitions offer high accuracy in measuring transceiver phase but tend to be slow. On the other hand, bSSFP-based acquisitions are favored for their acquisition speed, motion insensitivity, and automatic eddy current compensation due to balanced gradients. However, they are not without their challenges, such as non-constant phase in the presence of off-resonance and particularly near the notorious banding artifact, approximately pi-radian jumps.

The primary motivation behind the introduction of phase-based conductivity methods is the inherent limitation in obtaining B_1 magnitude data quickly. The conventional double-angle method [29], which requires the acquisition of two images with different flip angles and a long repetition time (TR), is often considered the gold standard but is hindered by the significant time investment it demands. Although advancements such as Actual Flip-angle Imaging (AFI) [30] and the Bloch-Siegert Shift-based method (BSS) [31] have contributed to improving acquisition efficiency, there is still room for further progress in this area.

1.3 Outline

This thesis primarily aimed to accelerate the acquisition of both phase and magnitude data for B_1, with the ultimate objective of facilitating the application of conductivity imaging in clinical settings. To achieve this goal, a variety of pulse sequences and reconstruction schemes were employed.

The acceleration of phase acquisition revolves around harnessing the potential of spiral imaging techniques within the context of MREPT. To further enhance the speed, implementation of various undersampling patterns are introduced. The combined outcome of these efforts is the remarkable achievement of obtaining B_1 phase data for the entire brain in less than a minute.

To substantially reduce the time required for B_1 magnitude image acquisition, a heavy undersampling scheme is introduced to the 3D Bloch-Siegert shift based

acquisitions. This approach is enhanced by the incorporation of total generalized variation (TGV) regularization, which improves image quality. Remarkably, this novel methodology enables the acquisition of B_1 magnitude images for the entire brain in less than 30 seconds.

2 Theoretical Background

This chapter provides a comprehensive overview of fundamental concepts in the field of Magnetic Resonance Imaging (MRI). The chapter is divided into five parts, each addressing a distinct aspect of MRI. The first section delves into the principles of Nuclear Magnetic Resonance (NMR), laying the groundwork for understanding how MRI works. The second part explores the core principles of MRI itself, including the generation of images and contrast. In the third section, standard clinical MRI pulse sequences that are commonly employed in medical imaging are presented. Moving forward, the fourth section delves into advanced techniques for accelerated data acquisition, which is vital for improving imaging efficiency. Finally, the fifth and last part of the chapter delves into the application of conductivity in MRI, highlighting its significance for diagnosis and treatment in the medical field. Together, these sections provide a solid foundation for comprehending the work presented in this thesis.

2.1 Nuclear Magnetic Resonance

This section provides the fundamentals of NMR. First, it discusses the properties of nuclear spin and macroscopic magnetization. Then, it covers the generation of NMR signals through Faraday's Law. After that, the components of the Bloch equation, namely precession, excitation, and relaxation, are explained.

2.1.1 Nuclear Spin

An intrinsic quantum property gives rise to a fundamental characteristic of the nucleus: Nuclei with an odd number of protons and/or an odd number of neutrons possess a property known as nuclear spin angular momentum, denoted by $\boldsymbol{I}$. The magnitude of the angular momentum vector, $|\boldsymbol{I}|$, can be written as $|\boldsymbol{I}| = \hbar\sqrt{I(I+1)}$, where $\hbar$ is Planck's constant ($\hbar = 1.05 \times 10^{-34}$) and I is the spin quantum number. The spin quantum number is an integer, if both number of protons and neutrons are odd; it is half integer if either number of proton or neutron is odd.

Isotope	Spin Quantum Number (I)	γ (MHz/T)	Abundance in Human Body
Hydrogen - ^{1}H	1/2	42.58	88 M
Sodium - ^{23}Na	3/2	11.27	80 mM
Phosphorus - ^{31}P	1/2	17.25	75 mM
Oxygen - ^{17}O	5/2	-5.77	17 mM
Fluorine - ^{19}F	1/2	40.08	4 μM

Tab. 2.1: List of selected nuclei, their spin quantum number (I), gyromagnetic ratios (γ), and abundance in human body.

The spin angular momentum can be imagined as similar to the circulation of an electrical current, consequently generating its magnetic moment. The direct relationship between nuclear spin angular momentum and magnetic moment can be expressed as:

$$\boldsymbol{\mu} = \gamma \boldsymbol{I} \tag{2.1}$$

The constant here, called gyromagnetic ratio, depends on the type of particle or nucleus. Frequently, instead of γ, $\gamma = \frac{\gamma}{2\pi}$ is also used in MRI field.

In theory, any nuclei meeting the $I \neq 0$ condition can be considered for use in NMR applications (the list of potential nuclei can be found in the Table 2.1). However, hydrogen remains the predominant choice in MRI due to two distinct advantages: its widespread abundance within the human body and having the largest gyromagnetic ratio among all stable nuclei.

2.1.2 Macroscopic Magnetization

While the magnitude of $\boldsymbol{I}$, and hence magnitude of $\boldsymbol{\mu}$ is intrinsic to the nuclei type, the orientation of $\boldsymbol{\mu}$ is not determined by the nuclei composition. Without an external magnetic field, there is no alignment of the magnetic moments of nuclei due to their random thermal motion. However, when we apply such a field, magnetic moment of a nuclei align with the external magnetic field. Moving forward, for the sake of simplicity and without introducing any loss of generality, we will assume the consistent application of the external magnetic field $\boldsymbol{B}$ with magnitude B_0 and directed along the z-axis.

The direction of the magnetic moment of a spin can only have discrete values with the application of the external field. Possibilities of the z-component of the magnetic moment are determined as, $\mu_z = \gamma m \hbar$, where m is the magnetic quantum number.

Since m can take values of $-I, I+1, ..., I-1, I$, the direction of a single spin must be one of the $2I+1$ of possibilities, shown in Figure 2.1.

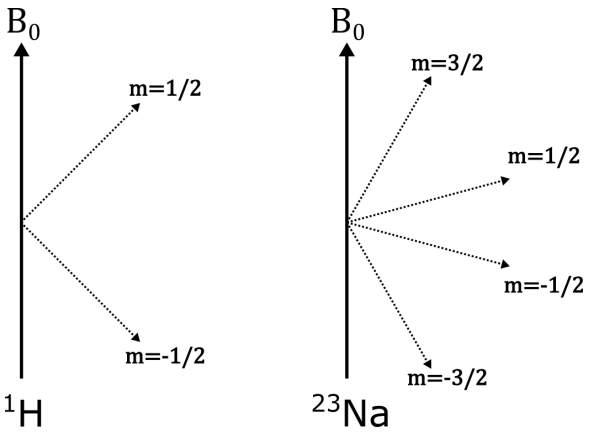

Fig. 2.1: Direction of nuclear magnetic moment vectors for two different nuclei, ^{1}H ($I = 1/2$) and ^{23}Na ($I = 3/2$).

Through quantum mechanics, the relationship between the potential energy E and the magnetic moment, μ is given as:

$$E = -\boldsymbol{\mu} \cdot \boldsymbol{B} = -\mu_z B_0 \tag{2.2}$$

Therefore, the potential energy is dependent on the direction of the magnetic moment. Energy difference between each direction can be stated as:

$$\Delta E = \Delta m \gamma \hbar B_0 \tag{2.3}$$

where Δm is the difference in magnetic quantum number between the two directions of the magnetic moment considered. This phenomenon of having different nuclear energy levels in accordance with their direction is known as *Zeeman effect*, shown in Figure 2.2. For instance, hydrogen has $I = 1/2$ and that leads to two energy states,

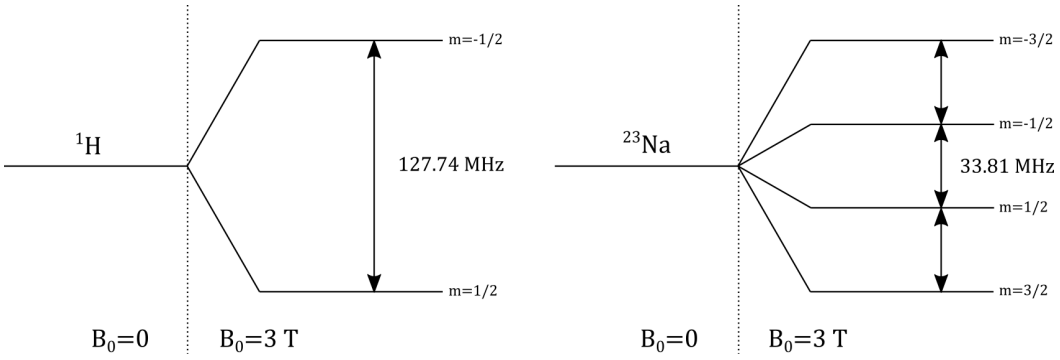

Fig. 2.2: Zeeman spliting for ^{1}H ($I = 1/2$) and ^{23}Na ($I = 3/2$). For ^{23}Na, consecutive energy level differences are equal to each other.

called parallel (n_+) and anti-parallel (n_-). The ratio of their population is:

$$\frac{n_-}{n_+} = e^{-\Delta E/kT} \tag{2.4}$$

where k is Boltzmann's constant and T is absolute temperature. For hydrogen, at room temperature, this ratio is about to be 0.999993, which states that there is only a difference of 7 per million nuclei (7 ppm) between each state. Though quite small, this difference in populations creates a macroscopic magnetization, $\boldsymbol{M}$, which is defined as $\boldsymbol{M} = \sum_{volume} \boldsymbol{\mu}$. The magnitude of $\boldsymbol{M}$, known as the equilibrium macroscopic magnetization, can be calculated as:

$$|\boldsymbol{M}| = M_0 = \frac{N\gamma^2\hbar^2 I_z(I_z+1)B_0}{3kT} \tag{2.5}$$

where N is the number of nuclear spins per volume.

2.1.3 Faraday's Law of Induction

Faraday's law of induction is a fundamental concept in electromagnetism that explains how a magnetic field can create an electric current in a circuit, a phenomenon known as electromagnetic induction. According to this law, the relationship between the flux through the coil, ϕ, and the electromotive force, ϵ, can be written as:

$$\epsilon = -\frac{d\phi}{dt} \tag{2.6}$$

Through the effect of reciprocity [32], we can relate magnetization with the flux, and hence, with the electromotive force as follows:

$$\epsilon = -\frac{d\phi}{dt} = -\frac{d}{dt}\int_{\text{volume}} \boldsymbol{B}_1^{\text{receive}}(r) \cdot \boldsymbol{M}(r,t)dV \tag{2.7}$$

where $\boldsymbol{B}_1^{\text{receive}}$ is the sensitivity of the receiver coil. Equation (2.7) highlights the importance of having magnetization changes over time to create an electromotive force and, in turn, a signal. To delve deeper into this concept, we'll first explore how magnetization changes work (*precession*), and then discuss the methods for inducing these changes (*excitation*), and finally reaching the equilibrium state once again (*relaxation*).

2.1.4 Precession

An external magnetic field prompts the creation of a macroscopic magnetization, $\boldsymbol{M}$, aligning itself in the same direction as the applied field, $\boldsymbol{B}$. When the magnetization is made to have a different direction than the external field, a phenomenon called "*precession*" will occur. This can be explained through classical mechanics, that is, a torque applied to a magnetic moment manifests itself as an angular momentum:

$$\frac{d\boldsymbol{I}}{dt} = \boldsymbol{\mu} \times \boldsymbol{B} \tag{2.8}$$

Multiplying both sides with γ leads to:

$$\frac{d\boldsymbol{\mu}}{dt} = \boldsymbol{\mu} \times \gamma\boldsymbol{B} \tag{2.9}$$

Considering macroscopic magnetization rather than a single moment and $\boldsymbol{B} = B_0\boldsymbol{k}$ where $\boldsymbol{i}, \boldsymbol{j}, \boldsymbol{k}$ are the unit vectors in x-,y-z- directions respectively:

$$\frac{d\boldsymbol{M}}{dt} = \boldsymbol{M} \times \gamma B_0\boldsymbol{k} \tag{2.10}$$

We can write this in a matrix form, which is:

$$\frac{d\boldsymbol{M}}{dt} = \begin{pmatrix} 0 & \gamma B_0 & 0 \\ -\gamma B_0 & 0 & 0 \\ 0 & 0 & 0 \end{pmatrix} \begin{pmatrix} M_x \\ M_y \\ M_z \end{pmatrix} \tag{2.11}$$

Solution of Equation (2.11) is simply:

$$\boldsymbol{M}(t) = \begin{pmatrix} M_x \\ M_y \\ M_z \end{pmatrix} = \begin{pmatrix} \cos(\omega_0 t) & \sin(\omega_0 t) & 0 \\ -\sin(\omega_0 t) & \cos(\omega_0 t) & 0 \\ 0 & 0 & 1 \end{pmatrix} \boldsymbol{M}(0) \tag{2.12}$$

where $\boldsymbol{M}(0)$ is the initial magnetization and $\omega_0 = \gamma B_0$. Equation (2.12) can be written in terms of rotation matrices, which is:

$$\boldsymbol{M}(t) = \boldsymbol{R_z}(\omega_0 t)\boldsymbol{M}(0) \tag{2.13}$$

Equation (2.13) describes the mechanism of the precession: The magnetization is rotating in clockwise direction, around the direction of the applied field (here, z-axis), at an angular frequency of ω_0 which is known as the *Larmor frequency*.

2.1.5 RF Excitation

To generate an NMR signal, it is imperative to perturb the magnetization from its equilibrium state so that receiver coils can detect changes in magnetic flux. This perturbation is achieved by applying an additional magnetic field, often represented as a radiofrequency magnetic (RF) pulse, denoted as $\boldsymbol{B_1}$, which is applied perpendicular to the static magnetic field, $\boldsymbol{B_0}$. For this purpose, an RF field can be created as:

$$\boldsymbol{B_1}(t) = B_1(t) \begin{pmatrix} \cos(\omega t) \\ -\sin(\omega t) \\ 0 \end{pmatrix} \tag{2.14}$$

where ω is the carrier frequency of the excitation. When we include such an RF field to Equation (2.10), it will become

$$\frac{d\boldsymbol{M}}{dt} = \boldsymbol{M} \times \gamma[\boldsymbol{B_1}(t)(\cos(\omega t)\boldsymbol{i} - \sin(\omega t)\boldsymbol{j}) + B_0\boldsymbol{k}] \tag{2.15}$$

With $\omega_0 = \gamma B_0$ and $\omega_1(t) = \gamma B_1(t)$ Equation (2.15) can be written as a matrix form similar to Equation (2.11):

$$\frac{d\boldsymbol{M}}{dt} = \begin{pmatrix} 0 & \omega_0 & \omega_1 \sin(\omega t) \\ -\omega_0 & 0 & \omega_1 \cos(\omega t) \\ -\omega_1 \sin(\omega t) & -\omega_1 \cos(\omega t) & 0 \end{pmatrix} \begin{pmatrix} M_x \\ M_y \\ M_z \end{pmatrix} \tag{2.16}$$

In order to simplify the calculations, we can switch to a rotating frame with rotation around the z-axis at a frequency of ω. In this rotating frame, Equation (2.15) becomes:

$$\frac{d\boldsymbol{M}}{dt} = M \times \gamma \left[B_1(t)\boldsymbol{i} + \left(B_0 - \frac{\omega}{\gamma} \right) \boldsymbol{k} \right] \tag{2.17}$$

and consequently, in matrix form:

$$\frac{d\boldsymbol{M}}{dt} = \begin{pmatrix} 0 & \omega_0 - \omega & 0 \\ -(\omega_0 - \omega) & 0 & \omega_1(t) \\ 0 & -\omega_1(t) & 0 \end{pmatrix} \begin{pmatrix} M_x \\ M_y \\ M_z \end{pmatrix} \tag{2.18}$$

With the choice of $\omega_0 = \omega$, the excitation is "*on-resonance*". With the assumption of constant RF field, $\omega_1 = \gamma B_1$, the solution of Equation (2.18) becomes:

$$\boldsymbol{M}(t) = \boldsymbol{R_x}(\omega_1 t)\boldsymbol{M}(0) \tag{2.19}$$

where $\boldsymbol{R_x}$ is a rotation matrix around the x-axis with an angular frequency of ω_1. With the initial magnetization along the z-axis, i.e. $\boldsymbol{M}(0) = \begin{bmatrix} 0 & 0 & M_0 \end{bmatrix}^T$, the time

evolution of the magnetization simply is a rotation of the magnetization along the x-axis:

$$\boldsymbol{M}(t) = \begin{pmatrix} 0 \\ M_0 \sin \omega_1 t \\ M_0 \cos \omega_1 t \end{pmatrix} \tag{2.20}$$

For general, time-varying $\boldsymbol{B_1(t)}$, Equation (2.19) becomes:

$$\boldsymbol{M}(t) = \boldsymbol{R_x} \left(\int_0^\tau \omega_1(t) dt \right) \boldsymbol{M}(0) \tag{2.21}$$

The amount of rotation of the magnetization, called *flip angle* (also called *tip angle*) is then dependent on the duration, τ, and the amplitude, B_1, of the applied RF pulse:

$$\begin{aligned} \alpha &= \gamma B_1 \tau && \text{for constant } B_1 \\ \alpha &= \gamma \textstyle\int_0^\tau B_1(t) dt && \text{for time-varying } B_1(t) \end{aligned}$$

2.1.6 Relaxation

Initially, the presence of the external magnetic field creates magnetization on the z-axis. This longitudinal component of the magnetization is referred to as $\boldsymbol{M_z}$. Simultaneously, the net magnetization within the x-y plane remains at zero due to the random phase distribution, forming what is known as the transverse component of the magnetization, $\boldsymbol{M_{xy}}$.

Following the initial excitation in MRI, the magnetization of the nuclear spins undergoes a process of realignment with the external magnetic field. During this time, the transverse magnetization, which was created by the excitation, gradually diminishes. Simultaneously, the longitudinal magnetization begins to regrow and return to its equilibrium state, aligning itself with the direction of the external magnetic field. The durations of these processes are governed by specific constants known as T_1 (longitudinal) and T_2 (transversal) relaxation times, which vary depending on the type of tissue or substance being studied. These relaxation times play a crucial role in determining the contrast and image quality in MRI, providing valuable insights into tissue properties and composition.

T_1 Relaxation

T_1 relaxation, sometimes called "*longitudinal*" or "*spin-lattice*" relaxation is characterized by the re-establishment of the equilibrium magnetization along the z-axis.

After excitation with an RF pulse, the spin system absorbs the RF energy. This excess energy is then released to the surrounding environment (the so-called lattice) and the spins go back to their original position leading to a re-growth of the longitudinal magnetization. This phenomenon is governed by the equation of:

$$\frac{dM_z}{dt} = -\frac{M_z - M_0}{T_1} \tag{2.22}$$

Solving Equation (2.22) results in:

$$M_z = M_0 + (M_z(0) - M_0)e^{-t/T_1} \tag{2.23}$$

Equation (2.23) characterizes the growing exponential nature of the longitudinal relaxation (see Figure 2.3). After an initial 90° pulse, at a time interval equal to the time constant T_1, M_z recovers approximately 63% of its original value. Furthermore, at a time approximately equal to 5 times T_1, the longitudinal magnetization is typically considered to have reached its stable equilibrium state.

T_2 Relaxation

T_2 relaxation, sometimes called "*transversal*" or "*spin-spin*" relaxation is characterized by the interactions of the spins. Brownian motion causes random fluctuations in the local magnetic field, resulting in loss of spin coherence and, in turn, loss of signal. This phenomenon is governed by the equation of:

$$\frac{dM_{xy}}{dt} = -\frac{M_{xy}}{T_2} \tag{2.24}$$

Solving Equation (2.24) results in:

$$M_{xy} = M_{xy}(0)e^{-t/T_2} \tag{2.25}$$

Equation (2.23) characterizes the decaying exponential nature of the transversal relaxation (see Figure 2.3). After the excitation, at a time interval equal to the time constant T_1, M_{xy} decays approximately 37% of its original value.

Relaxation times for tissues in the brain can be found in Table 2.2.

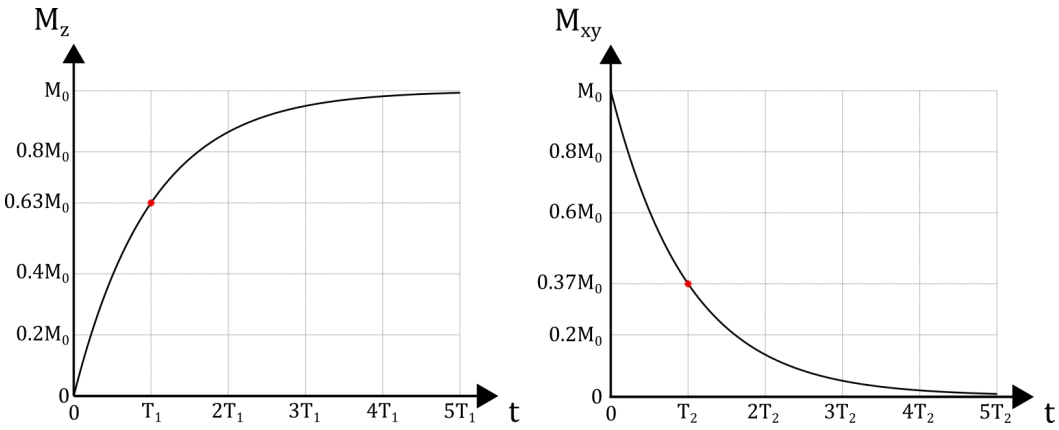

Fig. 2.3: Exponential growth of the longitudinal component (left) and exponential decay of the transversal component (right) after an initial 90° pulse. T_1 denotes the time where longitudinal component of the magnetization reaches 63% of its original value (M_0), while T_2 denotes the time where transversal component of the magnetization reach 37% of its original value.

Tissue	T_1 (ms)	T_2 (ms)
White Matter	790	90
Gray Matter	920	100
Cerebrospinal Fluid	4000	2000
Blood*	1200	50

Tab. 2.2: List of relaxation times for various tissue types at 3T. T_1 value is specified for arterial blood, and T_2 value is specified for venous blood [33].

T_2^* Relaxation

In the realm of NMR, it is commonly observed that the transversal relaxation process tends to occur at a faster rate compared to the intrinsic T_2 relaxation time. This phenomenon can be attributed to the influence of the external magnetic field, which plays a significant role in contributing to the decay of the transversal component. To gain a deeper understanding of this relationship, it is often assumed that the field inhomogeneity, which affects transverse relaxation, follows a Lorentzian spin distribution. This assumption serves as a foundation for establishing the interconnection between various transverse relaxation constants as follows:

$$\frac{1}{T_2^*} = \frac{1}{T_2} + \frac{1}{T_2'} \tag{2.26}$$

where T_2^* is called "*observed*" or "*effective*" transversal relaxation constant, and $T_2' = 1/(\gamma \Delta B_0)$ is the effect of transversal decay due to the presence of the off-resonance.

2.1.7 Bloch Equations

MRI relies on the influence of external magnetic fields to drive processes of excitation and relaxation. These effects can be captured in a single equation:

$$\frac{d\boldsymbol{M}}{dt} = \boldsymbol{M} \times \gamma \boldsymbol{B} + \frac{1}{T_1}(M_0 - M_z)\boldsymbol{k} - \frac{1}{T_2}(M_x \boldsymbol{i} + M_y \boldsymbol{j}) \tag{2.27}$$

This equation, also known as "*Bloch Equation*", governs the behaviour of the macroscopic magnetization, $\boldsymbol{M}(t)$ in the presence of a magnetic field, $\boldsymbol{B}$.

2.2 Magnetic Resonance Imaging

Magentic Resonance Imaging (MRI) is an imaging technique based on the principles of NMR that have been described in the previous section. In MRI, $\boldsymbol{B}(t)$ is a composite magnetic field, comprising three distinct components. The primary element is the static magnetic field, denoted as $\boldsymbol{B_0}$, responsible for establishing the initial magnetization and therefore relaxation. Additionally, there's the radiofrequency field, represented as $\boldsymbol{B_1(t)}$, employed for excitation purposes, and the gradient fields, marked as $\boldsymbol{G(t)}$, which play a pivotal role in spatial encoding within the MRI process. We have already covered the processes of excitation and relaxation, and now we're ready to delve into the realm of spatial encoding that will yield to imaging.

2.2.1 Gradient Fields

Up to this point, both the main static magnetic field, $\boldsymbol{B_0}$, and the radiofrequency field, $\boldsymbol{B_1}$, have been assumed to be spatially constant. Consequently, it was impossible to distinguish signals based on location. To address this challenge and enable spatial discrimination of signals, gradient coils have been introduced. These gradient coils generate linear gradient magnetic fields, which, when applied in conjunction with the main magnetic field, allow for precise spatial encoding of signals in MRI.

Let's consider the application of a gradient, G_x, in the z-axis, whose magnitude is changing along the x-axis. Then, the applied field will become $\boldsymbol{B} = (B_0 + G_x x)\boldsymbol{k}$, hence changing the frequency of the spins based on their location in the x-axis, i.e, $\omega(x) = \gamma(B_0 + G_x x) = \omega_0 + \gamma G_x x$. It is important to note that, all gradients

are pointed to the z-direction, however introducing field strength changes in their respective directions (x-, y- or z-).

As an example, let's assume we have 10 mT/m gradient strength across a 25 cm object. This gradient strength will create 106.45 kHz bandwidth over the object, with each frequency linearly linked to the position on the x-axis. This principle is the keystone for localizing signal that enables image acquisition.

In clinical settings, there are several limitations on gradients, namely *maximum gradient amplitude* and *maximum slew rate*. Higher limitations allow changing gradients in a rapid fashion, consequently, faster imaging. However, rapidly changing gradients can induce currents in human nervous systems, in accordance with the Faraday's Law. These unwanted currents can yield to *peripheral nerve stimulation (PNS)* which can be ranging from tingling/tapping sensation to painful muscle contractions [34], [35]. Maximum gradient amplitude and maximum slew rate limitations are determined for each MRI system, e.g. for MAGNETOM Tim Skyra systems (Siemens Healthcare GmbH, Erlangen, Germany) these limitations are 45 mT/m and 200 mT/m/ms respectively.

2.2.2 Signal Equation

With carefully selected assumptions (for more information [36]), the received time signal for a single slice can be expressed as:

$$s(t) = \int_x \int_y m(x,y) e^{-i\omega_0 t} e^{-i2\pi[k_x(t)x + k_y(t)y]} dxdy \tag{2.28}$$

where

$$k_x(t) = \frac{\gamma}{2\pi} \int_0^t G_x(\tau) d\tau \tag{2.29}$$

$$k_y(t) = \frac{\gamma}{2\pi} \int_0^t G_y(\tau) d\tau \tag{2.30}$$

and $m(x,y)$ is a function of NMR parameters, including spin density ($\rho(x,y)$), $T_1(x,y)$ and $T_2(x,y)$. In general, the main goal is to obtain a base-band signal $s_b(t) = s(t)e^{i\omega_0 t}$, to reconstruct an image, $I(x,y)$, which can be approximated by $m(x,y)$. In order to achieve this, 2D Fourier Transformation of $m(x,y)$ can be utilized:

$$M(k_x, k_y) = \int_x \int_y m(x,y) e^{-i2\pi[k_x(t)x + k_y(t)y]} dxdy \tag{2.31}$$

Equation (2.28) and Equation (2.31) are linked one-to-one, that is:

$$s(t) = M(k_x, k_y) \tag{2.32}$$

or

$$s(t) = M\left(\frac{\gamma}{2\pi}\int_0^t G_x(\tau)d\tau, \frac{\gamma}{2\pi}\int_0^t G_y(\tau)d\tau\right) \tag{2.33}$$

Equation (2.33) establishes a crucial relationship between the acquired signal and the desired image in MRI. It reveals that at any given moment, the acquired signal, s(t), directly corresponds to a 2D Fourier transformation of the underlying image $m(x, y)$ at a specific spatial frequency ($M(k_x, k_y)$). This relationship essentially charts a trajectory in what is known as *k-space*, a 2D Fourier transformation space where k denotes the spatial-frequency variable. The trajectory's path is determined by the time integral of the applied gradient fields. In MRI, the primary objective is to collect a comprehensive set of s(t) measurements that effectively span a significant portion of k-space. Through the subsequent process of inverse Fourier transformation, these measurements are converted into the desired image, enabling the creation of detailed and spatially resolved images.

2.2.3 Signal Localization

In the preceding section, we established the fundamental principles of 2D MRI imaging. The key steps involve exciting a specific slice in the imaged object and collecting a substantial portion of k-space data. Both of these steps crucially involve the use of gradient fields to spatially modulate the Larmor frequency of the object.

Slice Selection

In the absence of gradients, the B_1 field would excite all spins within the range of the excitation coil. To achieve selective excitation, an RF pulse with a modulation function is applied in the presence of a static gradient. This method ensures that only spins with resonant frequencies matching the frequency band of the RF pulse are excited, allowing for precise and controlled excitation in MRI.

Though we can have oblique slices in MRI, for the sake of simplicity, without the loss of generality, let's assume the slice is in the z-direction. The main goal is to excite a slice that has a thickness of Δz where its center is at $z = z_0$. In order to do that, the RF pulse bandwidth should cover the slice thickness, that is extending from

$z_0 - \Delta z/2$ to $z_0 + \Delta z/2$. With the constant gradient, G_z, the frequency profile over z-axis is: $f(z) = f_0 + \gamma G_z z$. That leads to the required bandwidth of the RF pulse:

$$\begin{aligned} BW_{rf} &= \Delta f \\ &= (\gamma G_z z_0 + \gamma G_z \Delta z/2) - (\gamma G_z z_0 - \gamma G_z \Delta z/2) \\ &= \gamma G_z \Delta z \end{aligned} \tag{2.34}$$

This equation highlights a crucial aspect of the process: To achieve uniform excitation throughout the imaging slice in the frequency domain, the RF pulse must be proportional to a rectangular function, $\sqcap(f/\Delta f)$. Through the aid of Fourier transformation, it can be shown that:

$$\begin{aligned} B_1(t) &\propto \mathcal{F}\left[\sqcap(f/\Delta f)\right] \\ &\propto sinc(\pi \Delta f t) \end{aligned} \tag{2.35}$$

Since $sinc$ functions extend to infinity, for practicality, time truncated versions are used in MRI scanners.

Frequency and Phase Encoding

After slice excitation, the aim is to obtain $m(x, y)$ from Equation (2.28). Consider a case where a constant gradient G_y is applied for a duration of τ after the RF pulse and then switched off. After that, another constant gradient, G_x is applied and the signal is acquired. In this case, Equation (2.28) becomes:

$$s(t) = \int_x \int_y m(x, y) e^{-i(\omega_0 + \gamma G_x x)t} e^{-i\gamma G_y y \tau} dx dy \tag{2.36}$$

The gradient G_x is referred to as the "*frequency-encoding*" gradient because it associates frequency with positions along the x-axis, determined by the strength of the gradient. On the other hand, the G_y gradient manifests as a phase contribution along the y-axis and is thus termed the "*phase-encoding*" gradient. By employing multiple pairs of these gradients, the entire k-space is comprehensively covered, enabling the acquisition of MRI images.

Pulse Sequence

A regular MRI scan consists of a scheduled series of RF and gradient pulses, which dictates how to acquire data in k-space during an MR measurement. This collection

of pulses, also called "*pulse sequence*", are used to fill the k-space. Once k-space is completely filled at the end of the scan, the data is processed mathematically to create the final image. In essence, k-space acts as the storage for raw data before the reconstruction of the image. Up to this point, continuous-time signals are discussed, however in reality, k-space is sampled in a discrete fashion as depicted in Figure 2.4.

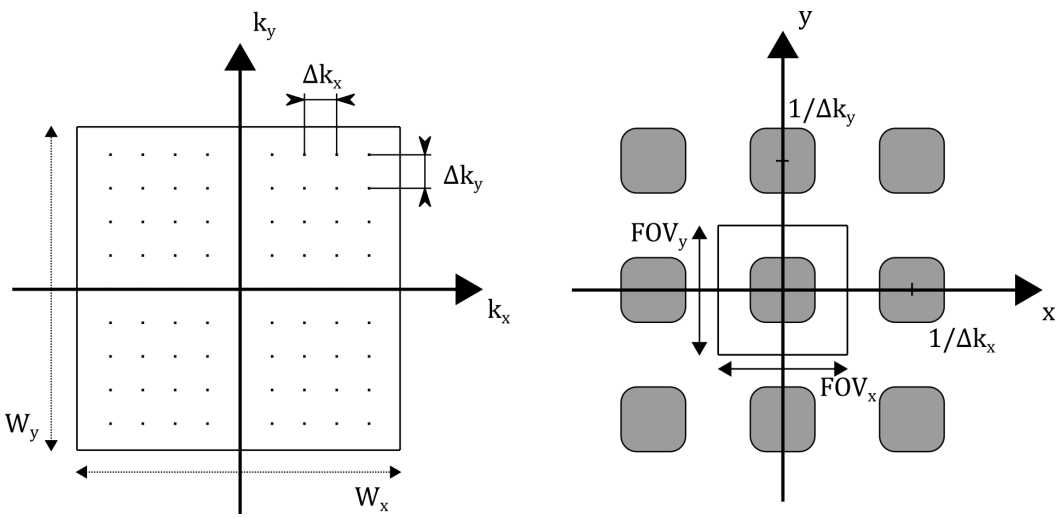

Fig. 2.4: Sampling in the k-space domain (left) and its corresponding replication in the image domain (right).

In a standard MRI, scanning is achieved via a repetitive fashion of (Figure 2.5):

- Slice selection, by using an RF pulse and slice selective gradients.
- Phase-encoding, by using various number of phase-encoding gradients to obtain different k-space lines
- Frequency encoding, by using frequency-encoding gradients to scan within the k-space line and at the same time to acquire data

By utilizing the steps above, k-space sampling is achieved. Mathematically, the sampled k-space can be expressed as:

$$\hat{M}(k_x, k_y) = M(k_x, k_y) \cdot \left(\frac{1}{\Delta k_x \Delta k_y}\right) {}^{2}\text{Ш}\left(\frac{k_x}{\Delta k_x}, \frac{k_y}{\Delta k_y}\right) {}^{2}\sqcap\left(\frac{k_x}{W(k_x)}, \frac{k_y}{W(k_y)}\right) \tag{2.37}$$

and the obtained sampled image is:

$$\hat{m}(x, y) = m(x, y) ** {}^{2}\text{Ш}(\Delta k_x, \Delta k_y) ** W(k_x)W(k_y)sinc(W(k_x)x)sinc(W(k_y)y) \tag{2.38}$$

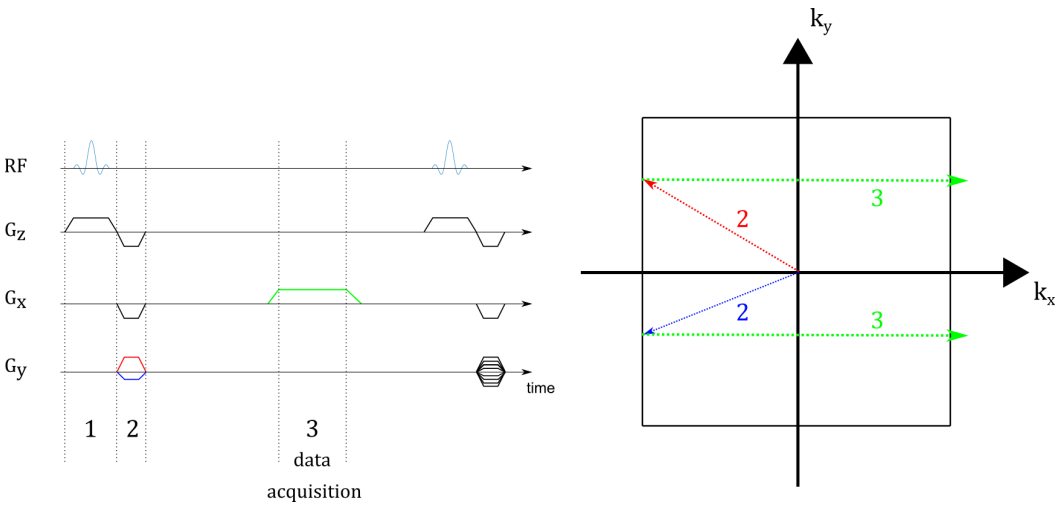

Fig. 2.5: A standard pulse sequence diagram and its corresponding k-space coverage. Step (1) is slice selection, achieved via an RF pulse and corresponding slice-selection gradient (here, in the z-direction). Step (2) is for preparation for the acquisition, traversing in the k-space is achieved via dephasing with x- and y- gradients. Step (3) is the data acquisition part. With the readout gradient (here, in the x-direction) samples along the specific line are obtained. This steps are repeated with the different phase-encoding gradients (here, in the y-direction) so that whole k-space coverage can be completed.

where ^2III is a 2D sampling function (also known as "*shah function*"), Δk_x and Δk_y are the sampling periods, $**$ is the 2D convolution operation, $W(k_x)$ and $W(k_y)$ are the k-space widths defined as:

$$\begin{aligned} W(k_x) &= 2\left(k_{x,max} + \frac{\Delta k_x}{2}\right) \\ W(k_y) &= 2\left(k_{y,max} + \frac{\Delta k_y}{2}\right) \end{aligned} \tag{2.39}$$

Image and k-space

From Equation (2.38), the convolution operation between $m(x, y)$ and the sampling operation pinpoints that we have replications of $m(x, y)$ across the image domain. In order to avoid overlapping replications ("*aliasing*"), the effective field of view (FOV) is determined by:

$$\begin{aligned} \text{FOV}_x &= \frac{1}{\Delta k_x} \\ \text{FOV}_y &= \frac{1}{\Delta k_y} \end{aligned} \tag{2.40}$$

Therefore, the FOV of an MRI image is determined by the sampling periods in k-space.

An MRI image consists of $N_{read} \times N_{pe}$ pixels where N_{read} is the number of samples in the readout (frequency encoding) direction and N_{pe} is the number of samples in the phase encoding direction. Therefore, the spatial resolution of an image can be stated as:

$$\begin{aligned} \delta_x &= \frac{FOV_x}{N_{read}} = \frac{1}{\Delta k_x N_{read}} = \frac{1}{W(k_x)} \\ \delta_y &= \frac{FOV_y}{N_{pe}} = \frac{1}{\Delta k_y N_{pe}} = \frac{1}{W(k_y)} \end{aligned} \tag{2.41}$$

Therefore, the spatial resolution of an MR image is determined by the sampling widths in k-space.

It's important to understand that k-space represents spatial frequency in MRI. This means that low spatial frequencies, which correspond to the center of k-space, determine the overall image contrast. Conversely, high spatial frequencies, located at the periphery of k-space, contain information about the image's sharpness and edge details. Figure 2.6 and Figure 2.7 illustrate this connection by using various masks applied to the acquired k-space data. This relationship forms the basis for various acceleration techniques, which will be discussed in the next chapters.

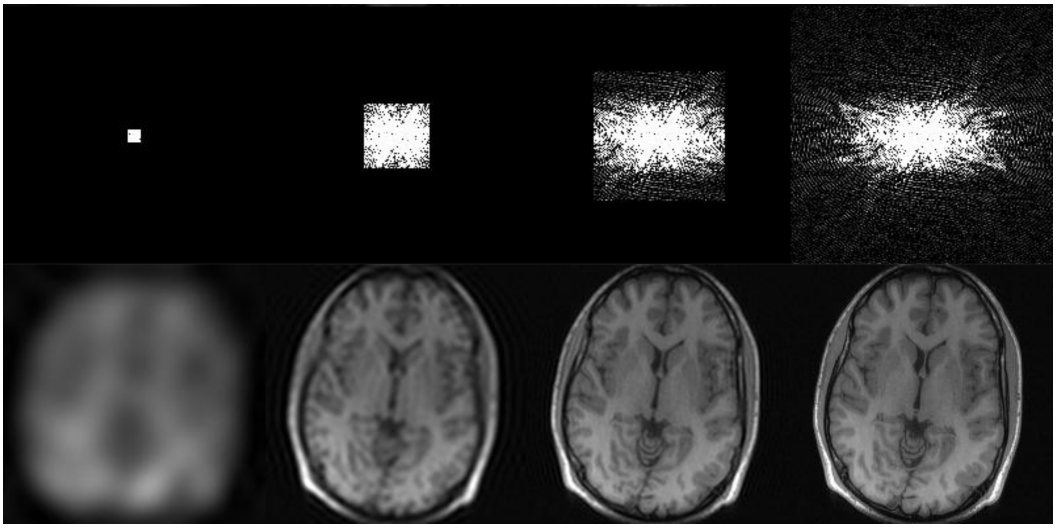

Fig. 2.6: Different central k-space data masks (top) and their corresponding images (below). The center of the k-space contains information related to the main contrast. The addition of high frequencies (k-space periphery) leads to better edge information.

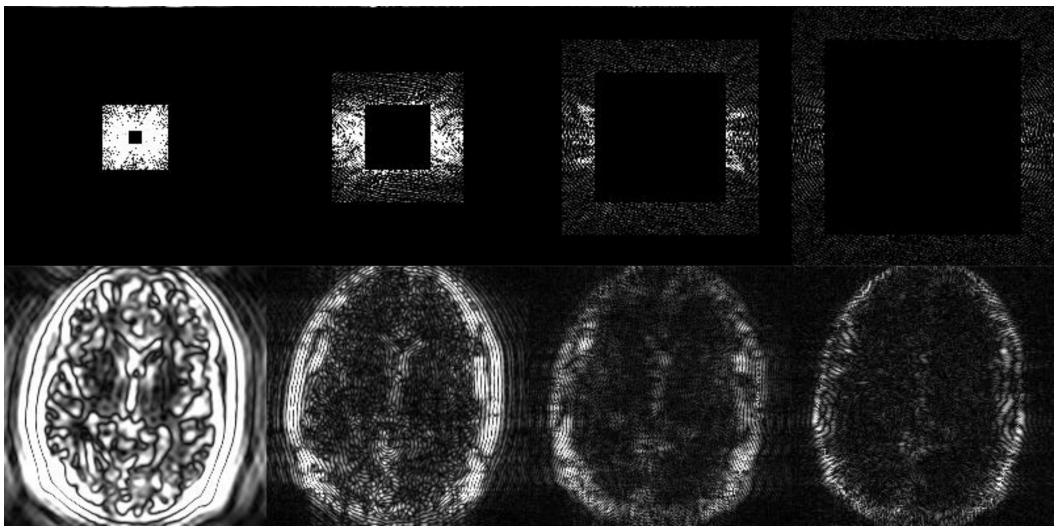

Fig. 2.7: Different peripheral k-space data masks (top) and their corresponding images (below). When moving to the periphery of the k-space the main image contrast is reduced, only edge information remains.

2.3 Standard MRI Pulse Sequences

2.3.1 Gradient Echo

In gradient echo imaging, the process can be broken down into a few key steps, which is illustrated in Figure 2.8. First, there is regular slice selection, where an RF pulse and a gradient are used to pick the specific slice to image. Then, we have dephasing, which involves activating gradients in the readout and phase encoding directions. With this step, resonance frequencies across the imaged object change, thus signal decay is accelerated. Finally, there is rephasing, where the readout gradient is reversed to undo the effects of dephasing, resulting in a "gradient echo". During this echo, the influence of the gradients is removed, revealing solely the T_2^* effect as shown in Figure 2.9.

Figure 2.8 illustrates two key user-controlled time-related parameters. *Echo time (TE)* defines the time between the center of the RF pulse and the acquired echo, while *repetition time (TR)* indicates the duration between consecutive RF pulses. Typically, TE is minimized to minimize the impact of T_2* decay and thus maximize the signal. When choosing TR, there are two approaches for handling remaining transverse component: opting for a long TR so that transversal relaxation is complete, or selecting a short TR and applying additional gradients for either spoiling, which eliminates remnants of transverse relaxation, or rewinding, which resets all magnetization to its initial state.

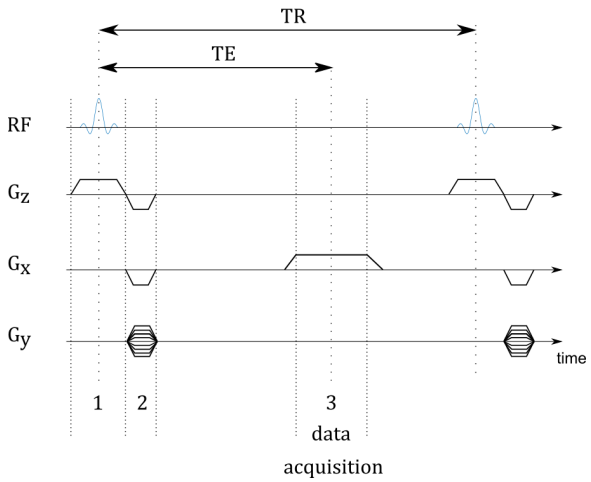

Fig. 2.8: A GRE pulse sequence diagram. Step (1) is the slice selection, achieved via an RF pulse and corresponding slice-selection gradient (here, in the z-direction). Step (2) is the preparation for the acquisition, traversing k-space is achieved via dephasing with x- and y- gradients. Step (3) is the data acquisition part. With the readout gradient (here, in the x-direction), samples along a specific k-space line are obtained.

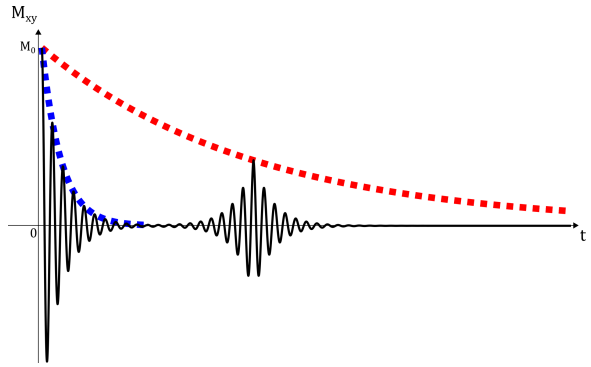

Fig. 2.9: T_2* decay (dotted red line), accelerated decay due to the introduction of gradients (dotted blue line) and obtained MRI signal. With the application of the readout gradient, dephasing is reverted and a gradient echo can be obtained.

2.3.2 Spin Echo

The spin echo, introduced by Edward Hahn in 1950 [37], predates the development of MRI technology and since then, spin-echo based sequences have remained fundamental in MRI advancements. In the spin echo, an extra RF pulse is applied at TE/2 to reverse T_2* effects and refocus dephased spins caused by B0 inhomogeneities. Hence, this echo primarily reflects T_2 decay, in contrast to gradient echo sequences influenced by T_2*. Typically, two RF pulse combinations of 90°-180°, are used, although variations exist. While Hahn initially proposed a pair of 90°-90° degree RF pulses, in 1954, Carr introduced the 90°-180° degree pulse configuration [38]. An examplary pulse sequence diagram is displayed in Figure 2.10.

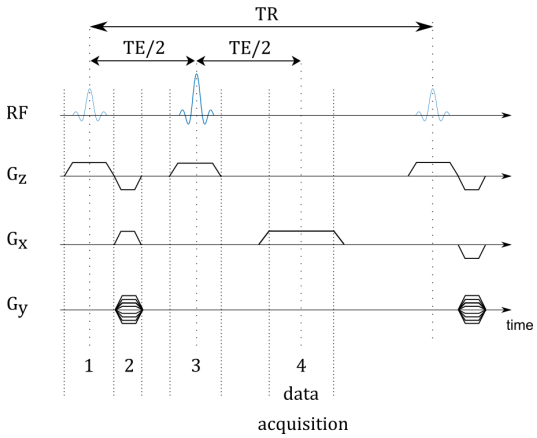

Fig. 2.10: A SE pulse sequence diagram. Step (1) is the slice selection, achieved via an RF pulse and corresponding slice-selection gradient (here, in the z-direction). Step (2) is the preparation for the acquisition, traversing k-space is achieved via dephasing with x- and y- gradients. Step (3) is the refocusing via a second RF pulse. Step (4) is the data acquisition part. With the readout gradient (here, in the x-direction), samples along a specific k-space line are obtained.

2.3.3 Balanced Steady-State Free Precession

One of the earliest MRI techniques, the groundwork for which was proposed by Carr in 1958 [39], is known as the balanced steady-state free precession (bSSFP). This technique involves the use of rapid and long sequences of RF pulses to bring the magnetization to a stable equilibrium. By employing balanced gradients (see Figure 2.11), where the net gradient area is zero, the influence of gradients for the next TR can be neglected. The resulting images offer several distinct advantages, including high SNR, rapid acquisition speed, motion insensitivity, and automatic compensation for eddy currents. However, bSSFP images exhibit mixed T_2/T_1 weighting and are susceptible to banding artifacts at specific off-resonance frequencies.

Steady state magnetization can be expressed as [40], [41]:

$$S = KM = KM_1 e^{-\mathrm{TE}/\mathrm{T}_2} e^{i\Omega \mathrm{TE}} \frac{1 - a e^{-i(\Omega + \Delta\Omega_{\mathrm{PC}})\mathrm{TR}}}{1 - b\cos{(\Omega + \Delta\Omega_{\mathrm{PC}})\mathrm{TR}}} \tag{2.42}$$

where

$$\begin{aligned} M_1 &= M_0 \frac{(1 - E_1)\sin\alpha}{1 - E_1\cos\alpha - (E_1 - \cos\alpha)E_2^2} \\ a &= E_2 \\ b &= E_2 \frac{1 - E_1 - E_1\cos\alpha + \cos\alpha}{1 - E_1\cos\alpha - (E_1 - \cos\alpha)E_2^2} \\ E_1 &= e^{-\mathrm{TR}/\mathrm{T}_1} \\ E_2 &= e^{-\mathrm{TR}/\mathrm{T}_2} \end{aligned} \tag{2.43}$$

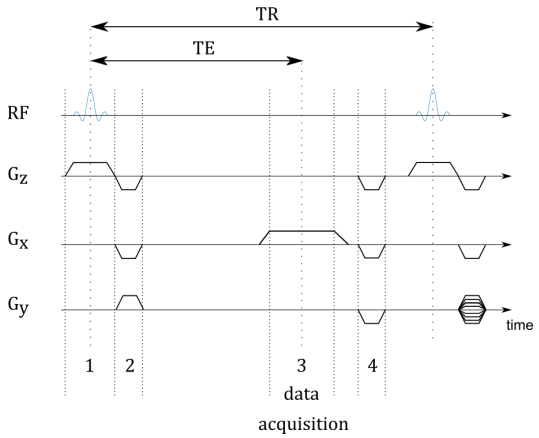

Fig. 2.11: A bSSFP pulse sequence diagram. Step (1) is the slice selection, achieved via an RF pulse and corresponding slice-selection gradient (here, in the z-direction). Step (2) is the preparation for the acquisition, traversing k-space is achieved via dephasing with x- and y- gradients. Step (3) is the data acquisition part. With the readout gradient (here, in the x-direction), samples along a specific k-space line are obtained. Step (4) is the rewinding part, via x-, y-, and z- gradients. All applied gradients are balanced, resulting in a net gradient area of zero within each TR.

K is the complex valued coil sensitivity, M_0 is equilibrium magnetization, α is the flip angle, Ω_{PC} is the user controlled phase increment, and Ω is the off-resonance term with $\Omega = 2\pi f_{\text{OR}}$ where f_{OR} is the off-resonance frequency.

Figure 2.12 illustrates the magnitude and phase of M with respect to the off-resonance frequency. The magnitude shows periodic behavior with a period of 1/TR. In the literature, the magnitude is typically divided into two regions: high-signal areas, known as *pass-band*, and the remaining areas are labeled *stop-band* regions [42]. Two key issues are associated with the magnitude: First, the magnitude varies even within the pass-band regions, dependent on factors like flip angle selection and the T_2/T_1 ratio of the specimen. Second, signal voids occur at frequencies of k/TR, where k is any integer. This void manifest themselves as dark bands in images, known as *banding artifacts*. Although the magnitude of M is quite complex in Equation (2.42), the phase is rather straight forward:

$$\angle(S) = \angle(K) + \angle(M) = \angle(K) + \Omega\text{TE} + \angle(1 - E_2 e^{-i(\Omega + \Delta\Omega_{\text{PC}})\text{TR}}) \tag{2.44}$$

The obtained phase depends on the transceiver phase ($\angle(K)$), the off-resonance and the T_2 value of the specimen. Around pass-band regions, the phase is changing almost linearly, however at frequencies of k/TR, jumps of approximately π-radian occur in phase.

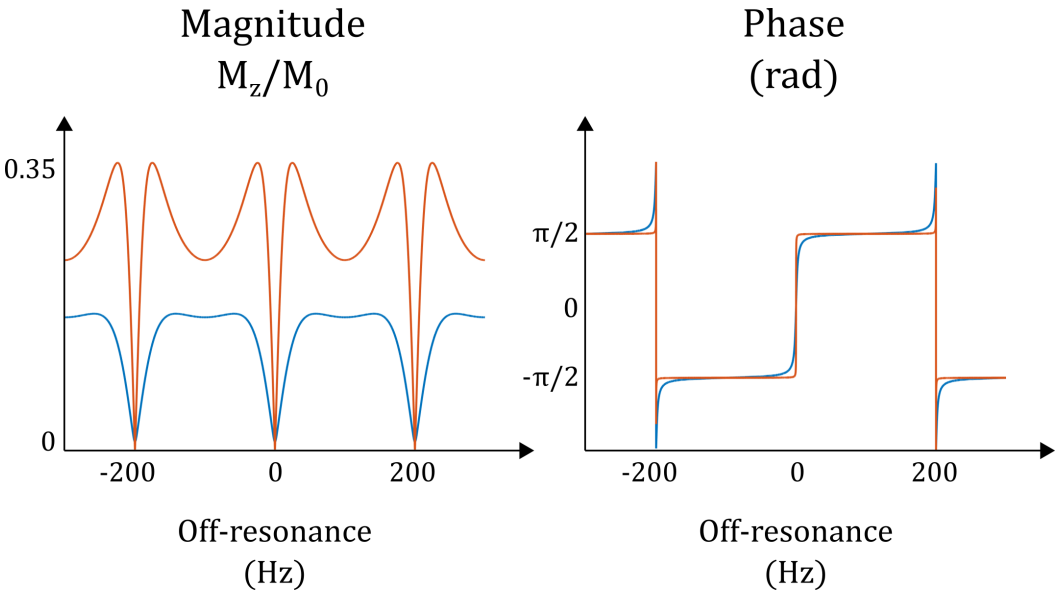

Fig. 2.12: bSSFP signal profiles with magnitude (left) and phase (right) for white matter (blue line) and CSF (orange line). Magnitude dips in the graph depicts the locations of the banding artifact, where in phase, approximately π-radian jumps occur.

2.4 Accelerated Data Acquisition

2.4.1 Parallel Imaging

Parallel imaging (PI) is a technique in MRI that capitalizes on the use of phased array receiver coils, by utilizing the spatial sensitivity of each individual receiver coil. This approach allows for accelerated data acquisition by undersampling k-space data, effectively reducing the number of phase-encoding steps. The resulting aliased image is subsequently resolved using the coil sensitivity information, leading to a significant reduction in scan time. The maximum achievable acceleration rate in PI is dependent on the number of available coils with distinct sensitivities. Overall, PI is a valuable method for enhancing MRI efficiency while maintaining image quality.

SENSE

SENSitivity Encoding (SENSE) is a parallel imaging technique developed by Pruessmann in 1999 [43]. This technique involves four key steps:

- Coil sensitivity maps for each coils are generated, by utilizing fast, low-resolution images.

- k-space data are undersampled by skipping phase-encoding lines with a user-selected undersampling ratio.
- Partial FOV images are reconstructed for each coil which are aliased due to undersampling.
- Matrix inversion is used to unfold superimposed pixels, producing a complete image.

GRAPPA

GeneRAlized Autocalibrating Partially Parallel Acquisition (GRAPPA) is a parallel imaging technique developed by Griswold in 2002 [44]. Similar to SENSE, this technique is using undersampling in phase-encoding direction. The main difference is that corrections are made in the image domain in SENSE while they are made in k-space in GRAPPA. This technique involves four key steps:

- Similar to the SENSE technique, the acquisition process in GRAPPA also involves undersampling k-space data by selectively omitting phase-encoding lines based on a user-defined undersampling ratio. However, central lines in k-space, known as "autocalibration signal (ACS)" lines, are fully sampled to provide reference data.
- ACS lines are used to calculate weighting factors for each coil, enabling the estimation of missing k-space points.
- Individual coil images are reconstructed, and these images are inherently corrected, free from aliasing artifacts.
- These individual coil images are combined to generate the final image.

Today, variety of usage area for SENSE and GRAPPA makes them the two primary parallel imaging techniques that are widely used in clinical routine [45].

SPIRiT

Iterative self-consistent parallel imaging reconstruction (SPIRiT), introduced by Lustig in 2010 [46], offers a unique approach to parallel imaging that combines the strengths of both the GRAPPA and SENSE techniques. Like GRAPPA, SPIRiT employs k-space kernels to recover missing k-space points, and similar to SENSE, it formulates image reconstruction as an inverse problem.

The SPIRiT reconstruction process begins with an initialization using zero-filled undersampled k-space data. Through a series of iterative steps, SPIRiT aims to find the most consistent solution with the calibration and data acquisition. Calibration consistency is established by enforcing agreement between every grid point and its surrounding neighborhood, expanding upon GRAPPA, which primarily focuses on consistency between synthesized and acquired points.

Data consistency plays a crucial role in SPIRiT, ensuring that acquired data points remain unchanged during calibration. The goal is to minimize the difference between the reconstructed and acquired data points for the acquired regions. The iterative process continues until a predetermined number of iterations is reached or the change between iterations falls below a specified threshold.

The final image output of SPIRiT is in a Cartesian grid, regardless of the sampling trajectory. Therefore, the flexibility of SPIRiT extends to non-Cartesian data reconstruction, making it a popular choice for various non-Cartesian sampling schemes.

2.4.2 Sampling Techniques

Accelerating data acquisition in MRI involves the application of advanced sampling techniques, among which Echo Planar Imaging (EPI), radial, and spiral sampling techniques are most commonly used. For these three sampling techniques, Figure 2.13 displays their pulse sequence diagrams and Figure 2.14 depicts their corresponding k-space trajectories.

In EPI, after slice selection, frequency encoding occurs by toggling the readout gradient sign while using small "blips" in the phase encoding direction after each acquired line in k-space (Figure 2.13). This results in a distinctive "zig-zag" k-space trajectory shown in Figure 2.14. Via EPI, the entire k-space can be traversed in a single TR (single-shot EPI) or over multiple TRs (multi-shot EPI), significantly reducing scanning time.

However, EPI does come with its share of challenges. It is susceptible to geometric distortion [47] due to off-resonance and eddy current effects, which can impact image accuracy. Additionally, EPI may exhibit ghosting artifacts when there is a mismatch between lines in the EPI trajectory [48]. Overcoming these challenges involves techniques like shimming [49], or taking reference scans [48]. Despite these challenges, EPI remains a valuable technique for rapid MRI acquisition.

In recent times, non-Cartesian trajectories, particularly radial and spiral trajectories, have gained popularity in the field of MRI. Radial sampling often employs center-out

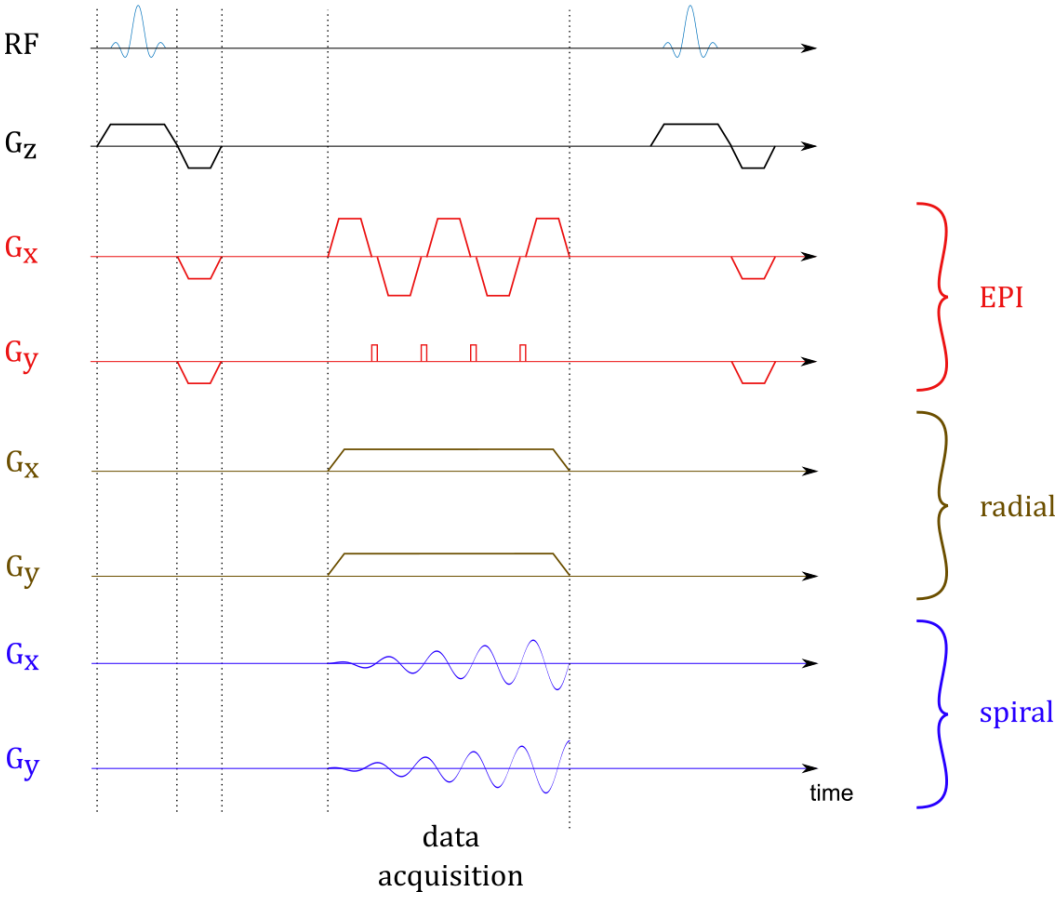

Fig. 2.13: Pulse sequence diagrams for EPI, radial, and spiral acquisitions.

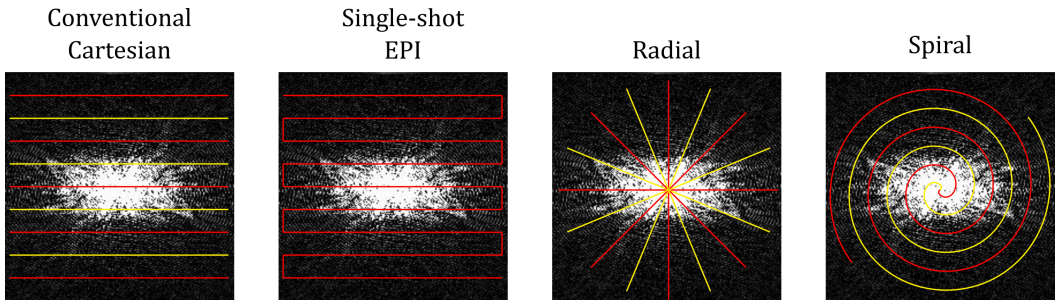

Fig. 2.14: Different sampling patterns for MRI acquisitions. Alternating colors represent data obtained in different TRs.

schemes, as illustrated in Figure 2.13 and Figure 2.14, offering the advantage of achieving very short echo times (TE) while rapidly reaching high spatial frequencies. The main advantage of this sampling schemes is motion insensitivity: The oversampled k-space center can be effectively utilized for motion detection and correction [50]. In addition to this, since radial sampling lacks a constant frequency

and phase-encoding direction, motion artifacts are not observed as ghosts but are instead distributed incoherently across the image [51]. However, radial sampling is notorious for its streaking artifacts, which can result from undersampling at the edges of the k-space or due to gradient non-linearities [52].

Spiral trajectories offer the advantage of a low TE, although they do not rapidly reach high spatial frequencies (Figure 2.13 and Figure 2.14). Instead, with longer readouts, they can efficiently cover the entire k-space very quickly, sometimes even within a single TR, resulting in faster imaging. However, spiral imaging is affected by the well-known halo artifacts, which manifest as rings near the periphery of the imaged object. There are several sources for this artifacts, including static off-resonance and concomitant fields, leading to blurring or ringing in the image [53]. Additionally, gradient imperfections can cause artifacts near the edge of the imaged object [53]. Various approaches can eliminate these unwanted effects, namely calculating gradient delays [54], correcting B_0 eddy currents [55], or simultaneously addressing off-resonance, trajectory errors, and concomitant field effects [56].

2.5 Conductivity in MRI

2.5.1 Electrical Properties of Tissues

Tissues, when exposed to a magnetic field, demonstrate characteristics of lossy dielectric materials. This behavior is fundamentally determined by their *electrical properties*, governed by two key factors: conductivity (σ) and permittivity (ε). These electrical attributes, taken together, constitute what is known as admittivity ($\gamma = \sigma + i\omega\varepsilon$).

It is worth emphasizing that tissue electrical properties vary significantly due to the diversity of electrolyte compositions within different tissues. Various examples for electrical properties of the several key tissues are highlighted in Table 2.3. In clinical studies, it is shown that these properties find utility in diagnosing conditions like ischemic and hemorrhagic strokes [23], as well as various forms of cancer, including breast [24] and prostate [57]. Furthermore, these electrical properties have the potential to play essential roles in therapeutic interventions, such as transcranial magnetic stimulation (TMS) [7], transcranial direct current stimulation [8], and radiofrequency (RF) ablation [9]. Therefore, knowledge of electrical properties can significantly aid in the diagnosis and treatment of a broad spectrum of medical conditions.

Tissue	Permittivity, ε_r	Conductivity, σ (S/m)
Blood	73.26	1.25
Brain - Gray Matter	73.71	0.59
Brain - White Matter	52.65	0.34
Cerebrospinal Fluid	84.19	2.14
Cervix	57.75	0.75
Liver	64.38	0.51
Lung - Deflated	63.83	0.58
Lung - Inflated	29.53	0.32

Tab. 2.3: Permittivity, ε, and conductivity, σ of various tissues in human body at 127 MHz [58].

2.5.2 Electrical Properties Imaging

Prior techniques for electrical properties imaging included Electrical Impedance Tomography (EIT) [12] and Magnetic Induction Tomography (MIT) [13], which involve the induction of currents using either surface electrodes (EIT) or external coils (MIT). However, these methods suffered from limitations, particularly in terms of spatial resolution within interior regions due to the reliance on surface potentials for measurements. To address these shortcomings, Magnetic Resonance Electrical Impedance Tomography (MREIT) was introduced [14]–[17]. MREIT employs surface electrodes to induce currents within the frequency range of 10 Hz to 10 kHz, and the resulting magnetic field was measured through MRI to reconstruct electrical property images. Nonetheless, a challenge in MREIT was to reduce the external applied current to safe levels while maintaining sufficient resolution.

A more recent approach, Magnetic Resonance Electrical Properties Tomography (MREPT), aims to image electrical properties of tissues by measuring the applied magnetic field, $\boldsymbol{B_1}$, induced at the Larmor frequency of the MRI system. Without any hardware requirement, this approach is only limited by the resolution of the measured $\boldsymbol{B_1}$ field. The concept of MREPT was first proposed by Haacke in 1991 [18], successfully applied by Wen in 2003 [19], and systematic research began with Katscher in 2009 [10].

2.5.3 Conductivity Reconstruction Techniques

Standard MREPT Reconstruction

From Maxwell's equations, the relationship between clockwise (left-handed) rotating component of the transmit RF magnetic flux density, B_1^+, and the admittivity of the object, $\gamma = \sigma + i\omega\varepsilon$, can be written as [59]:

$$-\nabla^2 B_1^+ = \frac{\nabla\gamma}{\gamma} \times (\nabla \times B_1^+) - i\omega\mu\gamma B_1^+ \tag{2.45}$$

where μ_0 is the magnetic permeability, σ is the conductivity, and ε is the permittivity of the imaged object. Since the solution of this problem is rather complex, several assumptions were made in order to simplify the equation [60]:

- **Locally constant electrical properties:** With the assumption of $\nabla\gamma(r) = 0$, the $\frac{\nabla\gamma}{\gamma} \times (\nabla \times B_1^+)$ term in Equation (2.45) can be ignored, leading to a much easier equation to solve. This assumption is widely known as the "*local homogeneity assumption*".

- **Constant vacuum permeability:** With the assumption of $\mu(r) = \mu_0$, the vacuum permeability is assumed throughout the object. Within the human body, this assumption holds fairly.

- **Isotropic γ:** At the Larmor frequency, anisotropy of the admittivity can be neglected in the human body.

With these assumptions, Equation (2.45) can be solved for admittivity quite easily:

$$\gamma = \frac{\nabla^2 B_1^+}{i\gamma\mu_0 B_1^+} \tag{2.46}$$

While Equation (2.46) is a common choice in the field of conductivity imaging, it comes with a notable limitation: Boundary artifacts are observed along tissue transitions due to the local homogeneity assumption. To address this concern, Hafalir introduced an alternative approach known as "*convection-reaction equation-based MREPT*", often referred to as "*cr-MREPT*" [61]. The formulation for this method can be expressed as:

$$\beta \cdot \nabla u + \nabla^2 H^+ u - i\omega\mu_0 H^+ = 0 \tag{2.47}$$

where $u = 1/\gamma$, $H^+ = \mu B_1^+$ and

$$\begin{aligned} \nabla u &= \begin{pmatrix} \frac{\partial u}{\partial x} \\ \frac{\partial u}{\partial y} \\ \frac{\partial u}{\partial z} \end{pmatrix} = \begin{pmatrix} \frac{1}{\gamma^2}\frac{\partial \gamma}{\partial x} \\ \frac{1}{\gamma^2}\frac{\partial \gamma}{\partial y} \\ \frac{1}{\gamma^2}\frac{\partial \gamma}{\partial z} \end{pmatrix} \\ \beta &= \begin{pmatrix} \frac{\partial H^+}{\partial x} - i\frac{\partial H^+}{\partial y} + \frac{1}{2}\frac{\partial H_z}{\partial z} \\ i\frac{\partial H^+}{\partial x} - \frac{\partial H^+}{\partial y} + \frac{i}{2}\frac{\partial H_z}{\partial z} \\ \frac{\partial H^+}{\partial z} - \frac{1}{2}\frac{\partial H_z}{\partial x} - \frac{i}{2}\frac{\partial H_z}{\partial y} \end{pmatrix} \end{aligned} \tag{2.48}$$

With the assumptions of $H_z = 0$ (valid for the central regions in the birdcage RF coil) and $\partial u/\partial z = 0$, the 2D version of Equation (2.48) can be written as:

$$F \cdot \bar{\nabla} u + \bar{\nabla}^2 H^+ u - i\omega\mu_0 H^+ = 0 \tag{2.49}$$

where,

$$\begin{aligned} \bar{\nabla} u &= \begin{pmatrix} \frac{\partial u}{\partial x} \\ \frac{\partial u}{\partial y} \end{pmatrix} \\ F &= \begin{pmatrix} \frac{\partial H^+}{\partial x} - i\frac{\partial H^+}{\partial y} \\ i\frac{\partial H^+}{\partial x} - \frac{\partial H^+}{\partial y} \end{pmatrix} \end{aligned} \tag{2.50}$$

While cr-MREPT successfully eliminates boundary artifacts, it introduces its own challenges: First, cr-MREPT methods has a specific artifact, which is known as the Low Convection Field (LCF) artifact. This artifact occurs in areas where the convective field, denoted as F, approaches zero, leading to spot-like artifacts. To mitigate the LCF artifact, various approaches were suggested, including utilizazion of inverse problem approach [62], combination of multi-channel data acquired through phased-array receive coils [63], introducing dielectric padding [64], and usage of multi-channel transmit systems [65]. Secondly, as detailed in the initial publication [61], cr-MREPT employed a 2D approach with a triangular mesh, disregarding alterations in the z-direction. Although this method demonstrates efficacy for phantoms with z-independence, its practicality for in-vivo imaging encounters challenges. The reasoning behind this is the adoption of a triangular mesh for 3D problems results in a substantial number of nodes, making the 3D solution computationally infeasible for conventional computers.

In order to solve either Equation (2.46) or Equation (2.47), both magnitude and phase of the transmit field, B_1^+, need to be acquired. However, both parts have their own problems:

- While several established techniques exist for acquiring the magnitude of the B_1^+ field, achieving this in a clinically feasible timeframe can pose a challenge.

- Unfortunately, the phase of the B_1^+ field cannot be measured directly by MRI. It is always combined with its counterpart, the reception field (B_1^-). Therefore, the phase of the transceiver field is obtained as the sum of both fields: $\phi_{tr} = \phi^+ + \phi^-$. In order to obtain ϕ^+, it is assumed that the phase of both fields are equal, so that $\phi_{tr} = 2\phi^+ = 2\phi^-$. This assumption, which is called the "*transceive phase approximation*", roughly holds for MR systems with quadrature body coil.

As conductivity calculations are predominantly influenced by the phase of B_1^+ and acquiring the magnitude of B_1^+ is time-consuming, MREPT methods that do not depend on magnitude information have emerged. These approaches are commonly referred to as "*phase-based*" MREPT techniques.

Phase-based MREPT Techniques

In order to avoid lengthy B_1^+ magnitude acquisitions, several phase-based MREPT techniques were developed. These methods are inherently free from the transceive phase approximation and do not require B_1^+ magnitude images. The standard phase-based approach is mathematically described as follows [60]:

$$\sigma = \frac{\nabla^2 \phi_{tr}}{2\mu_0 \omega} \tag{2.51}$$

There are couple of drawbacks of this method: It relies on the assumption of local homogeneity, resulting in the well-known boundary artifacts. Additionally, its utilization of low B_1^+ magnitude gradients can introduce errors, particularly near the periphery of the imaged object. To address the former limitation, Gurler and Ider introduced an alternative approach known as "*phase-based cr-MREPT*" [21]. This method leverages convection-reaction partial difference equations and eliminates the local homogeneity assumption. The formulation of this technique is as follows:

$$-c\nabla^2 \rho + (\nabla \phi_{tr} \cdot \nabla \rho) + (\nabla^2 \phi_{tr})\rho - 2\omega\mu_0 = 0 \tag{2.52}$$

where $\rho = 1/\sigma$ and c is the artificial diffusion term in order to prevent spurious oscillation.

2.5.4 B_1 Magnitude Acquisition

Double Angle Method Based Sequences

This method first suggested by Stollberger in 1996 [29]. In spin-echo imaging, the signal intensity at an arbitrary pixel, $I(r)$ can be expressed as:

$$I(r) = k\rho(r)S(\rho)\sin(\alpha(r))\sin(\beta(r)/2)R_1(\alpha(r),\beta(r),TR,TE,T_1(r))e^{-TE/T_2(r)} \tag{2.53}$$

where k is the system constant, $\rho(r)$ is the spin density, $S(r)$ is the coil sensitivity, α is the excitation angle, β is the refocussing angle, and $R_1(...)$ describes the longitudinal relaxation effect. In order to avoid complex calculations of the multipliers like system constant, the ratio of the two spin-echo images is taken for different flip angles. This ratio can be expressed as:

$$\frac{I_1(r)}{I_2(r)} = \frac{\sin(\alpha_1(r))}{\sin(\alpha_2(r))}\frac{R_1(\alpha_1(r),\beta_1(r),TR,TE,T_1(r))}{R_1(\alpha_1(r),\beta_1(r),TR,TE,T_1(r))} \tag{2.54}$$

With the selection of TR$\geq$5T$_{1,max}$, the longitudinal relaxation terms are equal to 1, and the ratio of the images depends only of the flip angle ratio. By selecting $\alpha_2 = 2\alpha_1$, this can be even further simplified:

$$\alpha_1(r) = \arccos\left(\frac{I_2(x)}{2I_1(x)}\right) \tag{2.55}$$

This technique is commonly known as the "*Double Angle Method*" and is widely acknowledged as the gold standard for obtaining B_1 magnitude. While this method is highly accurate, it is challenged by extended acquisition times due to the requirement of TR$\geq$5T$_{1,max}$.

Actual Flip-angle Imaging Based Sequence

This method first suggested by Yarnkh in 2006 [30]. In this method, two identical RF pulses with different TRs are used. With the assumption of ideally spoiled transversal magnetization, in steady state, longitudinal magnetization before each RF pulse can be written as:

$$\begin{aligned} M_{z,1} &= M_0\frac{1-E_2+(1-E_1)E_2\cos\alpha}{1-E_1E_2\cos^2\alpha} \\ M_{z,2} &= M_0\frac{1-E_1+(1-E_2)E_1\cos\alpha}{1-E_1E_2\cos^2\alpha} \end{aligned} \tag{2.56}$$

where $E_{1,2} = e^{TR_{1,2}/T_1}$ and M_0 is the equilibrium magnetization. Since the observed signals are proportional to the magnetization, their ratio becomes:

$$r = S_2/S_1 = \frac{1 - E_1 + (1 - E_2)E_1 \cos\alpha}{1 - E_2 + (1 - E_1)\cos\alpha} \tag{2.57}$$

By using first order Taylor series expansion ($e^{-x} = 1 - x$) and short $TR_{1,2}$, r can be further simplified:

$$r \approx \frac{1 + n\cos\alpha}{n + \cos\alpha} \tag{2.58}$$

where n is the ratio of the TRs (TR_2/TR_1). Therefore, the flip angle, α can be derived independent of the T_1:

$$\alpha \approx \arccos\frac{rn - 1}{n - r} \tag{2.59}$$

Bloch-Siegert Shift Based Sequences

This method first suggested by Sacolick in 2010 [31]. "*Bloch-Siegert shift*" characterizes the impact of off-resonance RF pulses on the nucleus. This RF pulse is carefully designed to change the precession frequency without causing excitation. This change leads to an additional phase, which depends on the strength of the B_1 field, and the degree of off-resonance in the RF pulse. The effective B_1 field can be described through Pythagorean theorem (Figure 2.15):

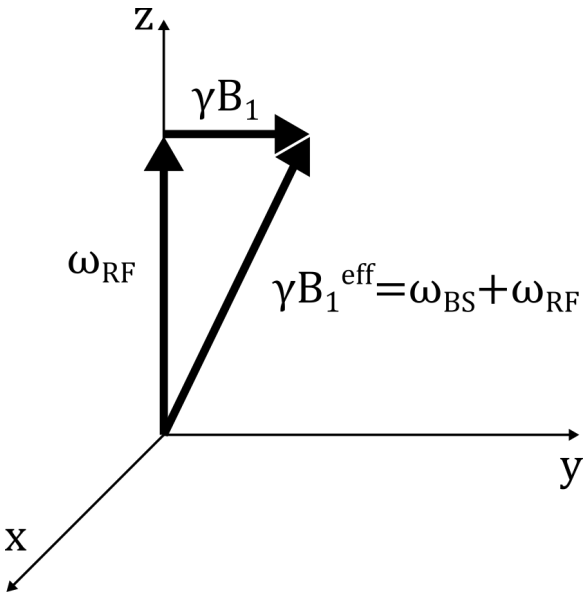

Fig. 2.15: The representation of the effective B_1 field in the Bloch-Siegert shift based method.

$$\gamma B_1^{eff} = \sqrt{\omega_{RF}^2 + \gamma B_1^2} \tag{2.60}$$

where ω_{RF} is the off-resonance value of the RF pulse. With the selection of $\omega_{RF} \gg \gamma B_1$,

$$(\omega_{BS} + \omega_{RF})^2 = \omega_{RF}^2 + (\gamma B_1)^2 \tag{2.61}$$

$$\omega_{BS} \approx \frac{(\gamma B_1)^2}{2\omega_{RF}} \tag{2.62}$$

With the addition of off-resonance effects, Equation (2.62) becomes:

$$\omega_{BS} \approx \frac{(\gamma B_1)^2}{2(\omega_{RF} + \omega_{B0})} \tag{2.63}$$

Therefore, the application of the off-resonance RF pulse can create a change in precession frequency, resulting in an additional phase. That phase can be calculated by:

$$\phi_{BS} = \int_0^T \omega_{BS}(t) = \int_0^T \frac{(\gamma B_1(t))^2}{2(\omega_{RF}(t) + \omega_{B0})} dt \tag{2.64}$$

Via Taylor series expansion and with the assumption of $\omega_{B0} \ll \omega_{RF}$:

$$\phi_{BS} \approx \int_0^T \frac{(\gamma B_1(t))^2}{2\omega_{RF}(t)} dt - \int_0^T \frac{(\gamma B_1(t))^2 \omega_{B0}}{2\omega_{RF}^2(t)} dt + O(\omega_{B0}^2) \tag{2.65}$$

In order to get rid of the ω_{B0} term, we can have two scans that have symmetric $\pm\omega_{RF}$ frequencies. ϕ_{BS} then becomes independent of B_0 by taking the phase difference of two scans. Hence:

$$\phi_{BS} = \int_0^T \frac{(\gamma B_1(t))^2}{2\omega_{RF}(t)} dt = B_{1,peak}^2 \int_0^T \frac{(\gamma B1, norm)^2}{2\omega_{RF}^2(t)} = B_{1,peak}^2 \cdot K_{BS} \tag{2.66}$$

$$B_{1,peak} = \sqrt{\frac{\phi_{BS}}{K_{BS}}} \tag{2.67}$$

where K_{BS} is a constant related to the RF pulse shape and $B_{1,peak}$ is the peak magnitude of B_1.

2.5.5 B_1 Phase Acquisition

Obtaining B_1 phase is achievable with most MRI sequences, but each approach comes with its unique advantages and drawbacks:

- Conventional gradient-echo methods are affected by off-resonance effects, whose phase is additive to the transceiver phase. To address this challenge, multi-echo gradient echo strategies can be adopted. Furthermore, these multi-echo gradient schemes can serve the dual purpose of acquiring conductivity

and susceptibility information simultaneously. However, both approaches utilize relatively long TR ($\sim$300 ms) durations, leading to slower acquisitions.

- Ultra-short Echo Time (UTE) or Zero Echo Time (ZTE) sequences can also be implemented for this purpose. With the center-out radial spokes, it has the advantage of being motion insensitive over multi-echo gradient echo schemes. However, those approaches suffer from streak artifacts, which will be amplified further through the Laplacian operation used in conductivity calculations.

- For the spin-echo based acquisitions, although Equation (2.53) is quite complicated, the phase contribution is only coming from the term k, whose phase is the pure transceiver phase. However, those acquisitions require long scanning time ($\sim$15-30 minutes), which limits their usage in clinical cases.

- Balanced steady-state free precession (bSSFP) is a popular choice for conductivity imaging due to its advantages, including high speed, high signal-to-noise ratio, motion insensitivity, and built-in eddy current compensation. However, it is susceptible to off-resonance effects. The phase acquired is not constant with respect to off-resonance, and at certain off-resonance frequencies, leading to the occurrence of well-known "*banding artifacts*". These artifacts cause an approximately π-radian phase shift around them, which can substantially distort the final conductivity image.

3 Methods

This chapter comprises two main sections. The first section delves into the technique developed in this work for accelerating B_1 magnitude acquisition, employing an undersampling scheme complemented by total generalized variation (TGV) regularization. The second section describes the method developed in this work for expediting B_1 phase acquisition, integrating variable density spiral acquisition with SPIRiT parallel imaging reconstruction.

3.1 Accelerating B_1 Magnitude

This section describes the development of the Bloch-Siegert based pulse sequence, the applied undersampling scheme, and the parameters of the MRI sequence. Additionally, it outlines the adaptation of total generalized variation for implementation in MREPT. Notably, parts of this section have been previously published in [66].

3.1.1 Data Acquisition

Bloch-Siegert Shift based Pulse Sequence Development

In order to obtain B_1 magnitude maps, a standard gradient echo (GRE) sequence is adapted by introducing a second off-resonance RF pulse immediately following the initial pulse. This secondary RF pulse is designed with a Fermi pulse shape which follows the formulation of:

$$B_1(t) = \frac{A_{RF}}{1 + e^{(|t|-a/b)}} e^{i\Delta\omega_{RF}t} \tag{3.1}$$

where A_{RF} is the amplitude, ω_{RF} is the off-resonance value for the RF pulse, a and b are the constants that define the shape of the RF pulse. An examplary pulse sequence diagram is shown in Figure 3.1.

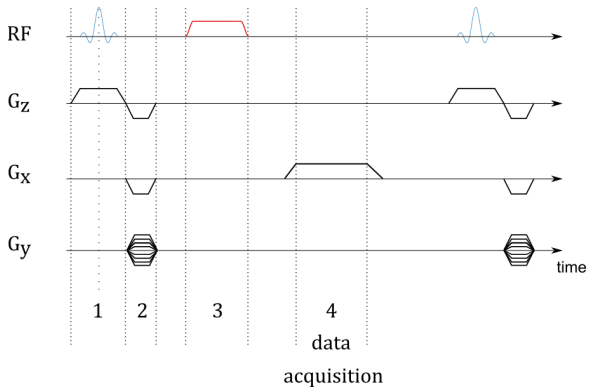

Fig. 3.1: Pulse sequence diagram for Bloch-Siegert shift based B_1 mapping method. The RF pulse in Step (3) (shown in red) is the off-resonance RF pulse that creates Bloch-Siegert shift.

Sampling Schemes

Taking advantage of the inherent smoothness of the B_1 magnitude map, which lacks high-frequency components, allows for efficient data capture when focusing on the central part of k-space. To test this, the acquired data were retrospectively undersampled, as shown in Figure 3.2. The dimensions were reduced from 128x128x32 to a highly accelerated 128x12x4 setup that can lead up to 85-fold speedup.

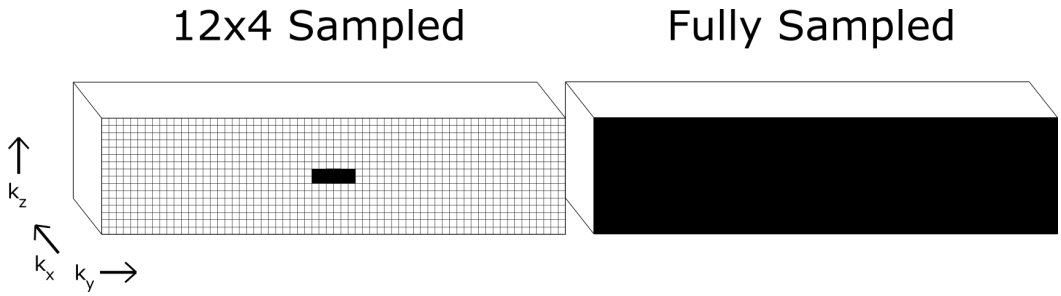

Fig. 3.2: k-space sampling patterns. Fully sampled data (128x128x32) are obtained first, then retrospectively 128x12x4 k-space data block is used.

MRI Scans

Experiments were conducted on a 3T scanner (Magnetom Tim Trio, Siemens Healthcare GmbH, Erlangen, Germany) using a 12-channel head coil.

To assess the efficacy of the undersampling scheme, an experimental phantom was fabricated, featuring two identical structures and a background section, as shown in Figure 3.3. This cylindrical phantom measured 16 cm in diameter and 20 cm in height, with uniform conductivity along the z-axis. The phantom's background area was filled with an agar-saline gel containing 20 g/L of agar, 2 g/L of NaCl,

Fig. 3.3: Constructed phantom that is used in the conductivity experiments.

and 0.2 g/L of $CuSO_4$. Within the phantom, the structures were formed by filling longitudinal cavities with a saline solution consisting of 6 g/L of NaCl and 0.2 g/L of $CuSO_4$, resulting in higher conductivity than the background region. These structures had a diameter of 3.5 cm. The expected conductivities are 0.35 S/m for the background area and 1.04 S/m for the structures [67].

To obtain B_1 phase, a 3D bSSFP pulse sequence was used. Sequence parameters were: TE/TR = 1.5/3 ms, FoV=256×256 mm, slice thickness = 2 mm, 32 averages, 32 slices, TA=6:32 min:s. To obtain B_1 magnitude, the aforementioned modified GRE sequence was used. Sequence parameters were: TE/TR=13/200 ms, FoV=256×256 mm, slice thickness = 2 mm, 32 slices, 8 ms long 4 kHz off-resonance Fermi pulse, TA=27:18 min:s.

3.1.2 Data Processing

To demonstrate the practicality of accelerating data acquisition, retrospective undersampling with total generalized variation (TGV) regularization was employed.

An open-source reconstruction framework [68] was utilized for TGV regularization, whose aim is to minimize the following term:

$$\frac{\lambda}{2}\sum_{j}^{N_c}\|P_+F(c_ju)-k_{j+}\|_2^2+\frac{\mu}{2}\sum_{j}^{N_c}\|P_-F(c_juv)-k_{j-}\|_2^2 \tag{3.2}$$

where λ and μ are regularization parameters, N_c is the number of the coils, P is the subsampling pattern, F is the Fourier operator, c_j is the coil sensitivity for the j-th coil, $k_\pm$ is the undersampled Fourier data corresponding to two different images ($I_\pm$) that are required for BSS based methods, where $I_\pm = |M|e^{j(\phi_0+\phi_{BS})}$, ϕ_0 is the background phase, ϕ_{BS} is the phase caused by Bloch-Siegert shift, u and v are the regularization terms, which are:

$$\begin{aligned} u &= |M|e^{j(\phi_0+\phi_{BS})} \\ v &\approx e^{-j2\phi_{BS}} \end{aligned} \tag{3.3}$$

Minimizing Equation (3.2) is accomplished via two steps of TGV and H1 regularization respectively:

$$\begin{aligned} \hat{u} &= \frac{\lambda}{2}\sum_{j}^{N_c}\|P_+F(c_ju)-k_{j+}\|_2^2+TGV_\alpha^2(u) \\ \hat{v} &= \frac{\mu}{2}\sum_{j}^{N_c}\|P_-F(c_juv)-k_{j-}\|_2^2+\frac{1}{2}\|\nabla v\|_2^2 \end{aligned} \tag{3.4}$$

Following Equation (2.67), the B_1 magnitude can then be obtained as:

$$B_{1,peak}=\sqrt{\frac{-\angle(\hat{v})}{2K_{BS}}} \tag{3.5}$$

The obtained $B_{1,peak}$ was then used as the magnitude of B_1 in the conductivity calculations. For this purpose, 2D standard MREPT and cr-MREPT reconstruction methods were employed. To eliminate the LCF artifact in the cr-MREPT technique, the data obtained with different coils were utilized together in the calculations [65].

Specific regions of interest (ROIs) encompassing the structures and the background were defined on magnitude bSSFP images. The segmentation was carried out using magnitude thresholding for each acquisition. Subsequently, the mean and standard deviation of conductivity values were calculated over these ROIs.

3.2 Accelerating B_1 Phase

This section describes the development of the variable density spiral pulse sequence, the applied undersampling scheme, and the parameters of the MRI sequence. Additionally, it outlines the data processing part, including SPIRiT parallel imaging reconstruction technique, for implementation in MREPT. Notably, parts of this section have been recently accepted for publication [69].

3.2.1 Data Acquisition

Spiral Trajectory based Pulse Sequence Development

To acquire B_1 phase images, a custom-built MRI pulse sequence utilizing spiral trajectories was developed. Spiral trajectory design is implemented in accordance with previous literature [70]. Users can select essential parameters through the MRI's user interface in the Sequence-Special tab, as illustrated in Figure 3.4. Those parameters are:

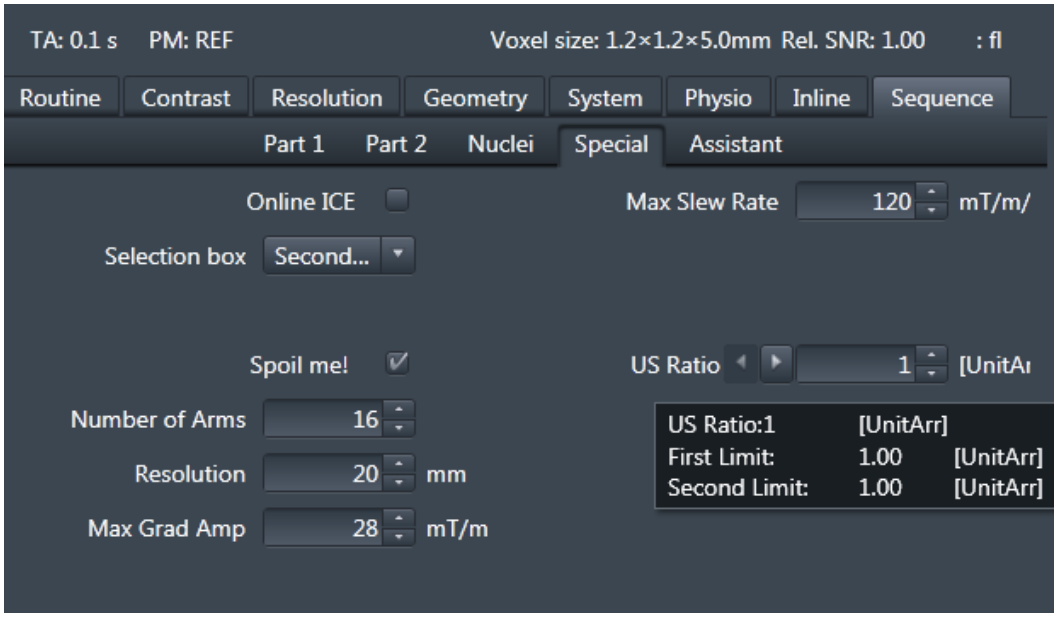

Fig. 3.4: User interface of the spiral trajectory based pulse sequence for B_1 phase data acquisition developed in this work.

- **Number of Arms:** This parameter sets the number of spiral interleaves needed to cover k-space, ranging from 1 to 90. Using fewer interleaves can reduce

the total acquisition time, but it may also introduce artifacts due to gradient imperfections or off-resonance effects.

- **Resolution:** This parameter sets the intended pixel size, ranging from 1 mm to 5 mm in intervals of 0.1 mm. Choice of a smaller pixel size enhances resolution but comes at the cost of increased TR and, consequently, a longer total acquisition time.

- **Gradient Limits:** To establish the gradient limits, two distinct constraints are taken into account. First, the *maximum gradient amplitude* can be tailored within the range of 20-35 mT/m, with 1 mT/m intervals. Second, the *maximum slew rate* can be adjusted between 20-180 mT/m/ms, with 1 mT/m/ms intervals. Higher limits result in faster image acquisition, but there is a risk of peripheral nerve stimulation in patients.

- **Undersampling Parameters:** We can set undersampling related parameters, namely *first limit (FL)*, *second limit (SL)*, and *undersampling ratio (UR)* here. The implemented sampling patterns allow complete coverage of the inner k-space region below the first limit, while the outer k-space region above the second limit is deliberately undersampled at the selected ratio. The region between the inner and outer sections is sampled with a gradually decreasing density. The first and second limit are defined relative to the maximum spatial frequency. In the user interface, UR from 1 to 5 can be selected, and FL and SL can be adjusted between 0.05 and 1 in intervals of 0.05.

MRI Scans

The experiments were conducted on a 3T scanner (Magnetom Skyra, Siemens Healthineers, Germany) equipped with a 16-channel head coil array.

In these experiments, spiral gradient-echo pulse sequences featuring both uniform and variable density patterns were employed. The phantom described in Subsection 3.1.1 (Figure 3.3) was imaged and in-vivo experiments of healthy volunteer were performed. The maximum repetition time (TR) for both the phantom and in vivo experiments was 6.9 ms, which decreased even further with undersampling. To achieve this, various undersampling schemes were employed via the user interface. Selection of examplary sampling patterns can be found in Figure 3.5. These patterns include combinations of FL/SL values such as 0.25/0.5 or 0.5/0.75, and UR options of 2, 3, or 4. Sequence parameters for the spiral acquisitions can be found in Table 3.1.

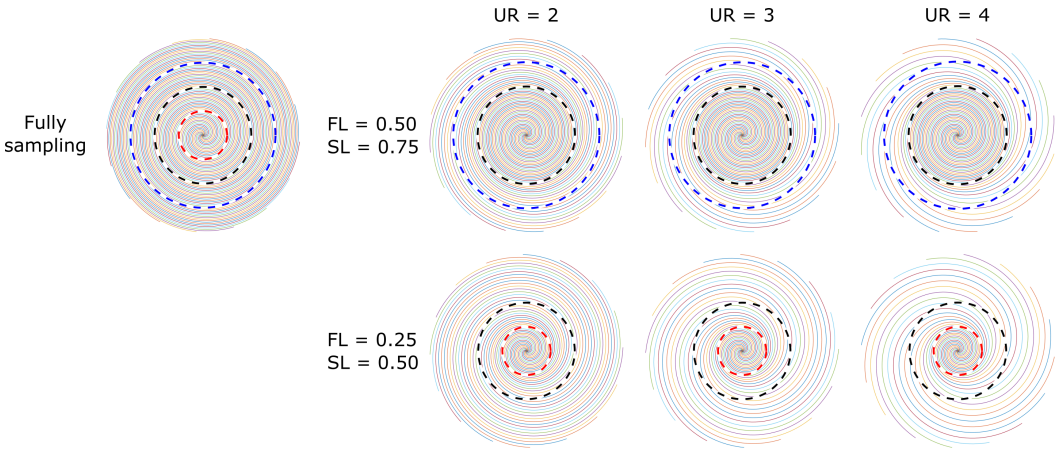

Fig. 3.5: k-space trajectories of different sampling schemes used in this study. Here, different colored circles represent different radii as a factor of the maximum spatial frequency, being red = 0.25, black = 0.5, and blue = 0.75. For each case, k-space is fully sampled within the first limit (FL), and various undersampling ratios (UR) are prescribed outside the second limit (SL). In the transition region between FL and SL, the undersampling ratio is varied linearly between full sampling and the prescribed UR.

Sampling Scheme	**Readout Time (ms)**	**TE/TR (ms)**	**Acquisition Time (s)**
Fully Sampled	3.97 (3.77)	1.12/6.9 (1.12/6.7)	56.52 (1.72)
UR/FL/SL=2/0.5/0.75	2.94 (2.80)	1.12/5.9 (1.12/5.7)	48.33 (1.46)
UR/FL/SL=3/0.5/0.75	2.55 (2.43)	1.12/5.5 (1.12/5.4)	45.06 (1.38)
UR/FL/SL=4/0.5/0.75	2.34 (2.22)	1.12/5.3 (1.12/5.2)	43.42 (1.33)
UR/FL/SL=2/0.25/0.5	2.45 (2.33)	1.12/5.4 (1.12/5.3)	44.24 (1.36)
UR/FL/SL=3/0.25/0.5	1.90 (1.81)	1.12/4.8 (1.12/4.7)	39.32 (1.20)
UR/FL/SL=4/0.25/0.5	1.62 (1.54)	1.12/4.6 (1.12/4.5)	37.68 (1.15)

Tab. 3.1: Sequence parameters for in vivo (phantom) experiments. Other parameters are: slice thickness = 2.5 mm, flip angle = 15°, number of slices = 32 (1), resolution = 2×2 mm^2, FOV = 270×270 (256×256) mm^2, spiral interleaves = 16, maximum gradient amplitude = 28 mT/m, maximum slew rate = 120 mT/m/ms, number of averages = 16.

To comparatively illustrate the performance of spiral acquisitions, an additional bSSFP acquisition with a Cartesian readout from the same volunteer was acquired. Sequence parameters were: TE/TR = 1.55/3.10 ms, FOV = 270×270 mm^2, matrix size = 128×128, FA = 15°, number of averages = 4, number of slices = 32, total duration = 50.8 s.

The standard volumetric shimming provided by the manufacturer was conducted at the start of the scanning session and remained unchanged throughout the acquisitions.

3.2.2 Data Processing

To ensure the robust reconstruction of the spiral acquisitions, the SPIRiT reconstruction framework was utilized. Specifically, a conjugate gradient algorithm for non-Cartesian SPIRiT within the image domain was implemented. In this context, a total of 15 iterations were set, employing a 5x5 kernel and a 20x20 calibration area. To combine the phase data obtained from different receive channels, the Virtual Reference Coil Approach was employed. Additionally, a Gaussian filter was applied to the transceive phase data, with a kernel size of 5x5x3 (or 5x5 in the case of 2D acquisition).

For the phantom measurements, a 2D version of the phase-based cr-MREPT technique, which doesn't account for variations in the z-direction, was employed. On the other hand, for the in vivo measurements, the complete 3D formulation was utilized.

To assess the quality of the spiral-based conductivity images, specific regions of interest (ROIs) were defined on magnitude images of both spiral trajectory and bSSFP acquisition. These ROIs encompassed the structures in the phantom images and the cerebrospinal fluid in the in vivo measurements. The segmentation was carried out using magnitude thresholding for each acquisition. Subsequently, the mean and standard deviation of conductivity values were calculated over these ROIs.

4 Results

This chapter is divided into two main sections. The first section explores the conductivity results of a phantom experiment, comparing comductivity images obtained with fully sampled and undersampled B_1 magnitude images. TGV regularization is applied to the undersampled version to enhance image quality. Phantom results demonstrate a remarkable 85 times acceleration without compromising image quality, enabling 3D acquisition within just 30 seconds. The second section delves into the conductivity results of both phantom and in-vivo experiments using a variable density spiral-based pulse sequence. The SPIRiT parallel imaging technique is employed to improve image quality. Results indicate that a single slice with multiple averages can be obtained within a second, while achieving whole brain coverage within a minute. Notably, parts of this chapter have been previously published in [66] and recently accepted for publication [69].

4.1 Accelerating B_1 Magnitude

bSSFP magnitude and phase images of the phantom are shown in Figure 4.1 for two different slices. bSSFP phase is used as transceiver B_1 phase for conductivity calculations for both standard and cr-MREPT technique. Meanwhile bSSFP magnitude depicts the location of the structure regions and is used for masking purposes.

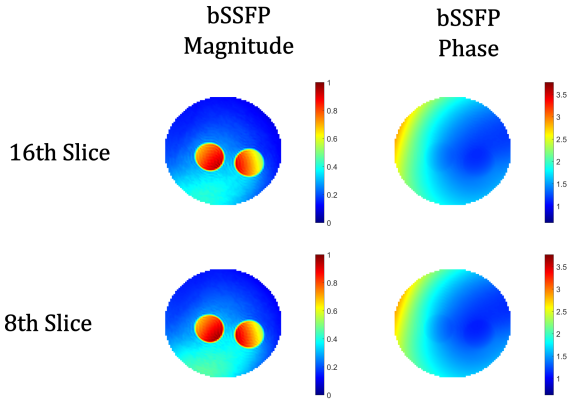

Fig. 4.1: For two different slices, magnitude and phase of the bSSFP image. The phase image is used as a B_1 phase, while the magnitude image depicts the location of the structure region.

B_1 magnitude obtained via Bloch-Siegert shift based technique is shown in Figure 4.2. The 12x4 sampled version was obtained in a retrospective fashion from the fully sampled version. The ratio of undersampled and fully sampled B_1 maps are at maximum of $\pm 2\%$ in the 16th slice and $\pm 5\%$ in the 8th slice. The deviation is especially higher along the boundaries of the structure region, due to the missing high-frequency components in the undersampled version.

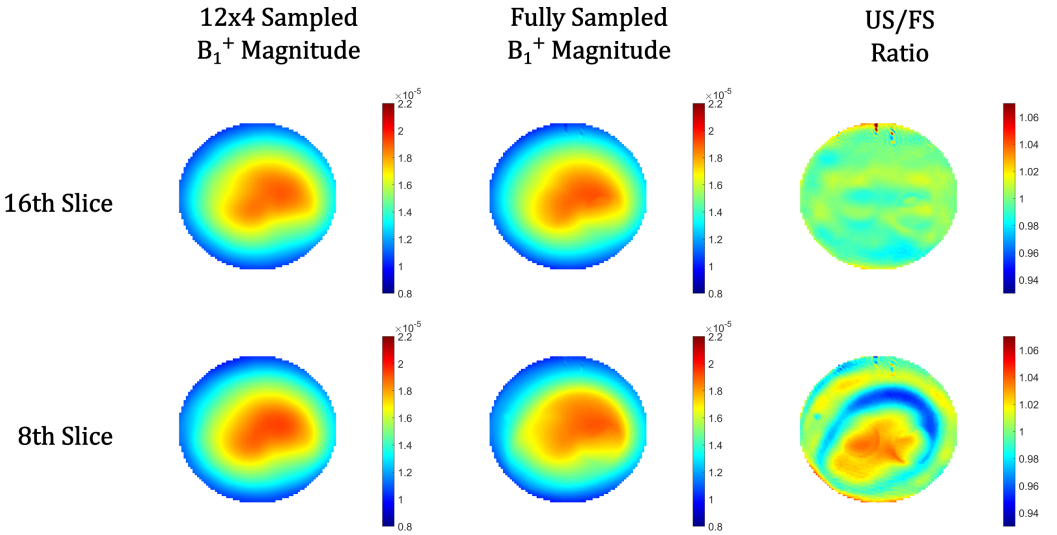

Fig. 4.2: For the phantom experiment, retrospectively undersampled B_1 magnitude images (first column), fully sampled B_1 magnitude images (second column) and their ratios (third column) for two different slices.

Figure 4.3 shows the conductivity results obtained via standard MREPT reconstruction technique. Although this method is suffering along the structure boundaries due to the local homogeneity assumption, there are no visible conductivity differences between undersampled and fully sampled versions.

Figure 4.4 displays the conductivity results obtained via cr-MREPT reconstruction technique. Local homogeneity assumption related artifacts are not present and similar conductivity results are obtained, regardless of the choice of the sampling or location of the slice.

Table 4.1 and Table 4.2 present the conductivity values resulting from various sampling patterns and reconstruction techniques for two distinct slices. The lower standard MREPT conductivity observed in the background region is attributed to negative values near structure boundaries, stemming from the local homogeneity assumption. Notably, sampling with a 12x4 block and the fully sampled case yield nearly identical results across both slices and reconstruction techniques. Conse-

quently, 85 times acceleration (resulting in whole brain coverage in less than 30 seconds) without compromising the image quality is achievable via this undersampling scheme.

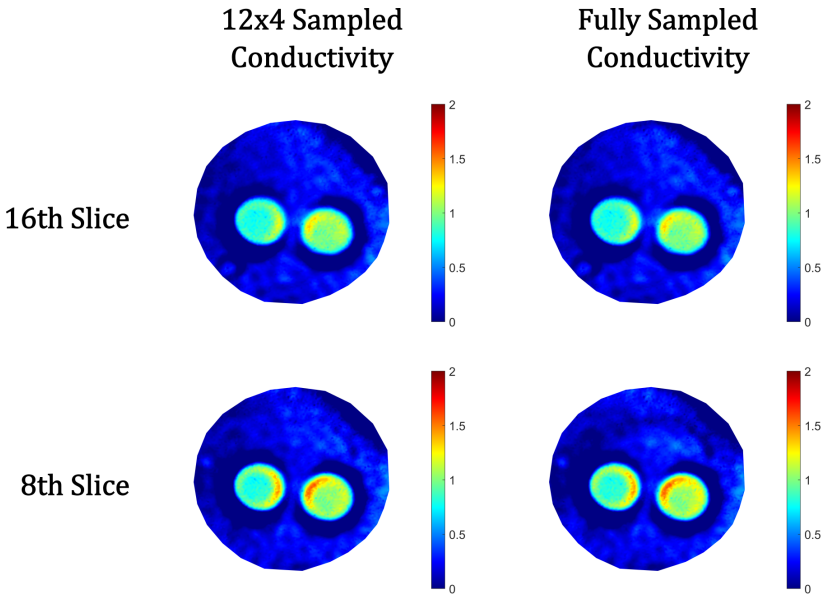

Fig. 4.3: Conductivity maps, obtained with retrospectively undersampled B_1 magnitude images (left column) and fully sampled B_1 magnitude images (right column) via standard MREPT method for two different slices.

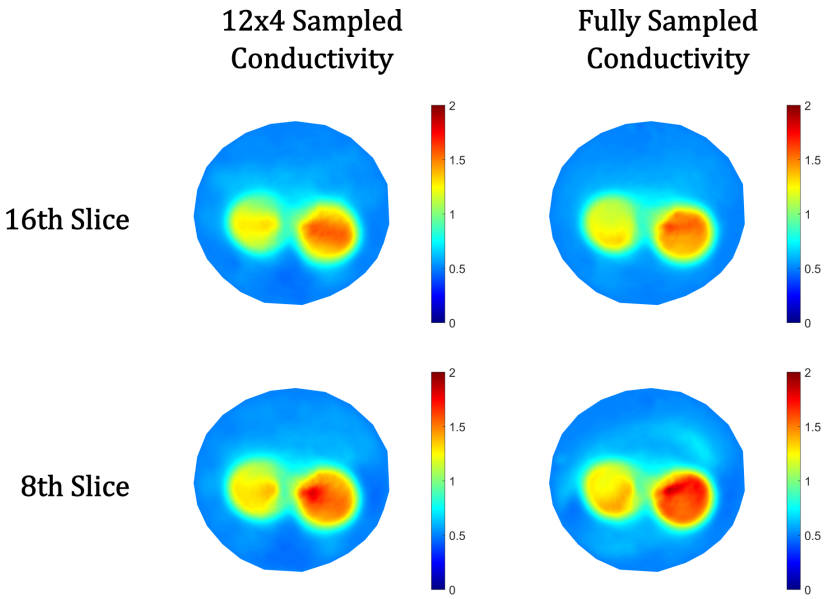

Fig. 4.4: The conductivity maps, obtained with retrospectively undersampled B_1 magnitude images (left column) and fully sampled B_1 magnitude images (right column) via cr-MREPT method for two different slices.

Conductivity Values (S/m) for 16th Slice (mean±std)			
Sampling Scheme	**Reconstruction**	**Background**	**Structures**
Fully Sampled	std-MREPT	0.103±0.240	0.811±0.309
Fully Sampled	cr-MREPT	0.600±0.140	1.286±0.159
12x4 Block	std-MREPT	0.106±0.237	0.812±0.307
12x4 Block	cr-MREPT	0.598±0.143	1.272±0.177

Tab. 4.1: Mean and standard deviation of conductivity values with different sampling patterns and reconstruction techniques for the 16th slice.

Conductivity Values (S/m) for 8th Slice (mean±std)			
Sampling Scheme	**Reconstruction**	**Background**	**Structures**
Fully Sampled	std-MREPT	0.087±0.257	0.929±0.341
Fully Sampled	cr-MREPT	0.629±0.174	1.418±0.192
12x4 Block	std-MREPT	0.088±0.262	0.899±0.345
12x4 Block	cr-MREPT	0.614±0.172	1.350±0.176

Tab. 4.2: Mean and standard deviation of conductivity values with different sampling patterns and reconstruction techniques for the 8th slice.

4.2 Accelerating B_1 Phase

4.2.1 Phantom Measurements

The feasibility of the undersampled spiral trajectories in conductivity imaging was first demonstrated using phantom measurements. Figure 4.5 depicts the phase difference maps obtained from acquisitions with different undersampling schemes. Here, the reference image was designated as the phase map obtained from the fully sampled acquisition. The differences observed between each case are relatively small, with a maximum mean squared error below 10^{-3}.

Figure 4.6 displays conductivity images obtained through the phase-based cr-MREPT technique. A magnitude image from the fully sampled case is also included as a visual reference. The conductivity differences between the undersampling schemes and the fully sampled case are depicted in Figure 4.7. Notably, the fully sampled case exhibits a halo artifact that becomes less prominent by introducing undersampling. However, as the undersampling ratio increases, residual aliasing artifacts hinder the overall image quality, as observed for the case of UR/FL/SL = 4/0.25/0.50. In Table 4.3, the mean and standard deviation values using different sampling schemes are reported.

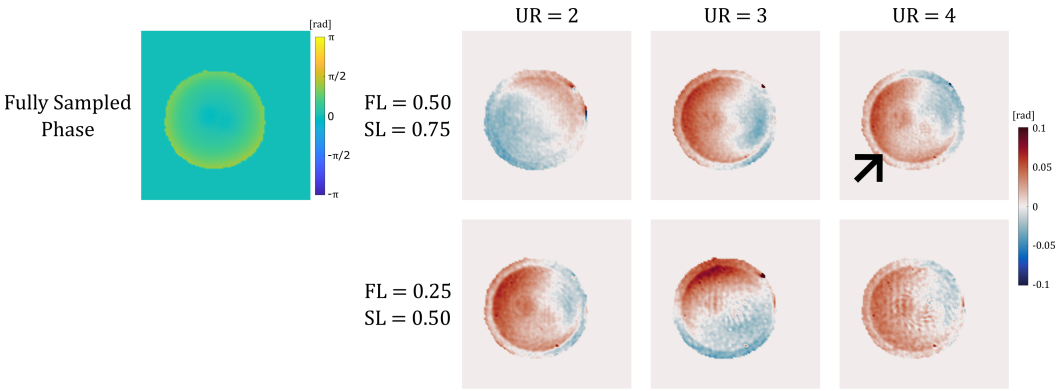

Fig. 4.5: Fully sampled phase and phase differences of each undersampled scheme with respect to fully sampled case. The effect of halo-artifact is clearly visible (black arrow) and with excess amount of undersampling, the whole phase image is distorted. However, overall differences are very small, with a maximum mean squared error below 10^{-3}.

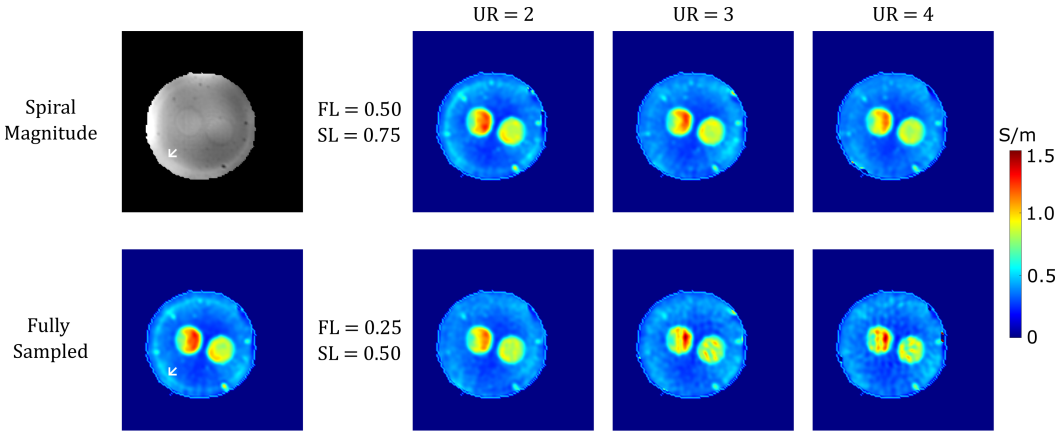

Fig. 4.6: Conductivity images obtained through the phase-based cr-MREPT technique in phantom measurements. The fully sampled spiral magnitude image is also displayed as a visual reference to facilitate the identification of structures within the imaging region. It is observed that the fully sampled spiral acquisition is afflicted with halo artifact (depicted with a white arrow), which are effectively mitigated by the implementation of undersampling. However, it should be noted that in cases of extreme undersampling, such as those with low FL/SL and high UR, the entire conductivity image is susceptible to distortions.

The conductivity images obtained with varying numbers of averages are shown in Figure 4.8. Here the sampling scheme of UR/FL/SL = 3/0.5/0.75 was selected for illustration purposes. It is noteworthy that even with a single average with an acquisition time below 0.1 second, the structures are clearly discernible. While the addition of more averages leads to the expected improvement in quality, there is almost no observable difference in image quality after eight averages. In Table 4.4, the mean and standard deviation values for the various numbers of averages are

reported. Notably, the standard deviation does not vary after eight averages. Consequently, this acquisition scheme enables the acquisition of a single slice in well under a second.

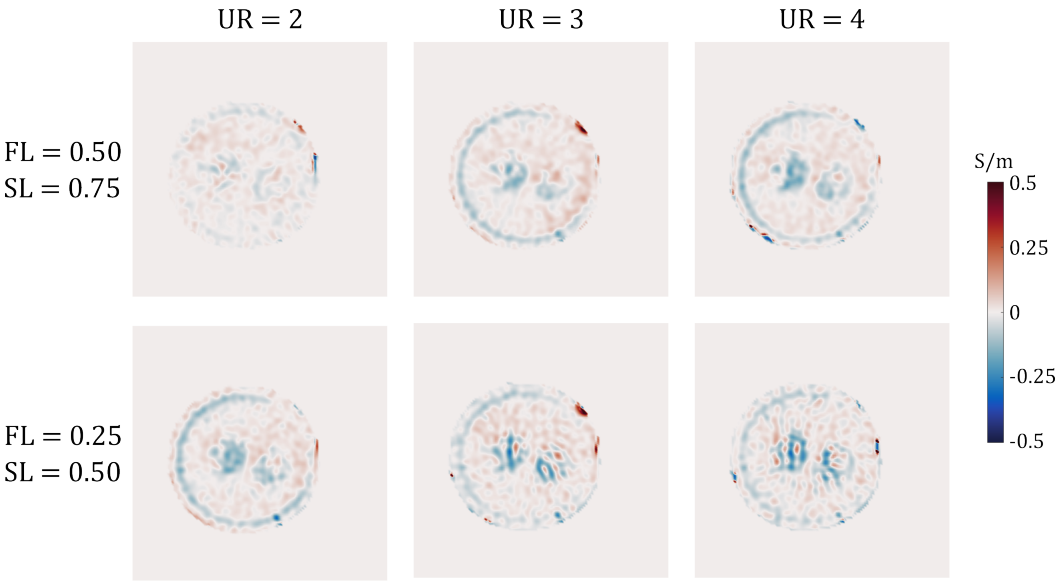

Fig. 4.7: Conductivity differences of different undersampling schemes with respect to the fully sampled acquisition. Mainly, the error arises from two different sources: Halo artifacts are mitigated by using undersampling; and residual aliasing artifacts that distorts the conductivity images due to the excessive undersampling.

Conductivity Values (S/m) for Phantom Experiment with Different Sampling Schemes (mean±sd)		
Sampling Scheme	**Background**	**Structures**
Fully Sampled	0.378±0.089	0.913±0.160
UR/FL/SL=2/0.5/0.75	0.380±0.092	0.902±0.155
UR/FL/SL=3/0.5/0.75	0.381±0.082	0.887±0.139
UR/FL/SL=4/0.5/0.75	0.374±0.082	0.856±0.125
UR/FL/SL=2/0.25/0.5	0.374±0.075	0.861±0.127
UR/FL/SL=3/0.25/0.5	0.378±0.087	0.857±0.158
UR/FL/SL=4/0.25/0.5	0.372±0.091	0.852±0.159

Tab. 4.3: Mean and standard deviation of conductivity values obtained from phantom experiments using different sampling schemes. The results are in close agreement with the expected conductivity values of 0.35 S/m for the background and 1.04 S/m for the structures. Introduction of undersampling effectively reduces the standard deviation. However, extreme undersampling with low limits and high undersampling ratio can lead to increased standard deviation.

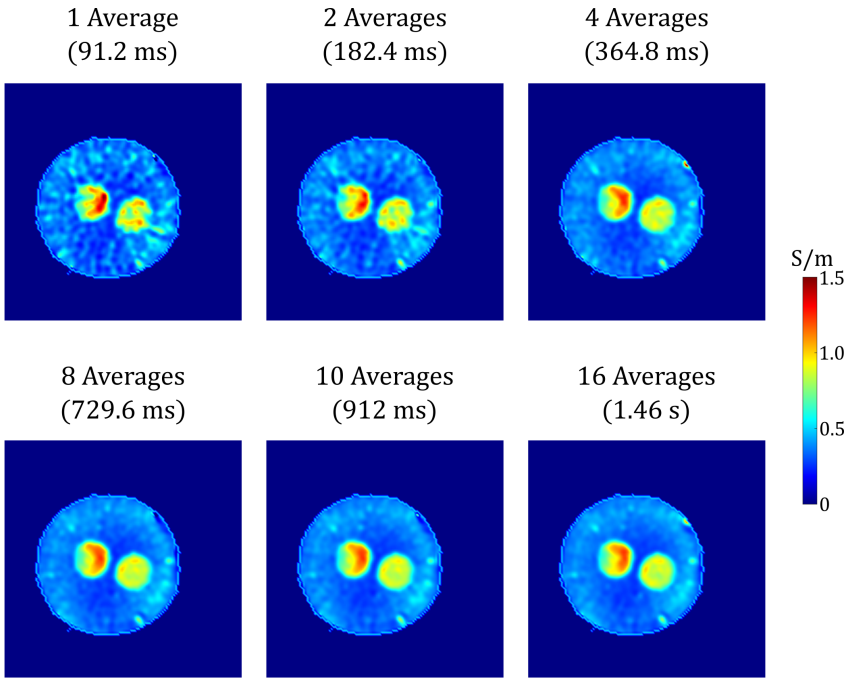

Fig. 4.8: Conductivity images obtained with varying numbers of averages (1, 2, 4, 8, 10, and 16). Even with only one average, structures are visible, albeit with poorer image quality. As the number of averages increases, the image quality improves as expected. However, noticeable differences in image quality become minimal after 8 averages.

Conductivity Values (S/m) for Phantom Experiment with Different Averages (mean±sd)		
Averages	**Background**	**Structures**
1	0.372±0.101	0.881±0.198
2	0.376±0.094	0.886±0.159
4	0.381±0.090	0.890±0.145
8	0.378±0.082	0.890±0.141
10	0.379±0.082	0.886±0.142
16	0.381±0.082	0.887±0.139

Tab. 4.4: Mean and standard deviation of conductivity values with different number of averages. It is noteworthy that after 8 averages, both standard deviations does not change substantially with the increment of number of averages.

4.2.2 In Vivo Brain Measurements

Figure 4.9 illustrates the in vivo conductivity values obtained through the phase-based cr-MREPT method, where the magnitude image of the fully sampled case is used as a visual reference. The conductivity images clearly display prominent structures, such as cerebrospinal fluid (CSF). However, similar to the conductivity images obtained from the phantom, cases with low limits and high undersampling ratios lead to image distortions.

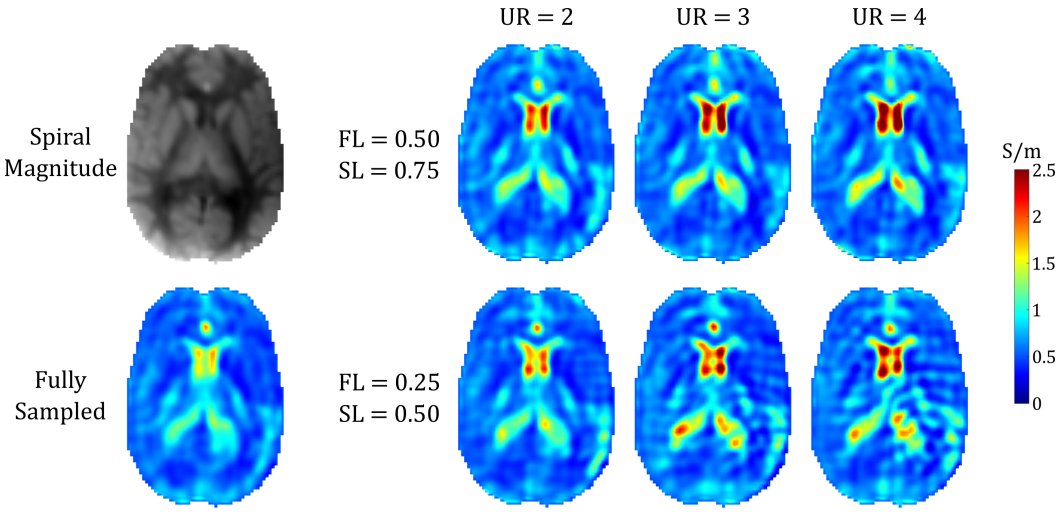

Fig. 4.9: Conductivity maps derived from a healthy volunteer using various sampling schemes. The proposed spiral trajectories demonstrate the ability to obtain conductivity maps, albeit with residual artifacts evident across tissues and boundaries at higher undersampling ratios. Nevertheless, all measurements successfully delineate prominent structures, such as the cerebrospinal fluid (CSF).

Figure 4.10 shows the comparison of conductivity maps obtained from the 14th slice of bSSFP and spiral acquisitions, alongside with their magnitude and phase images as a reference. For spiral case, the sampling scheme of UR/FL/SL = 3/0.5/0.75 was chosen. While the effects stemming from the off-resonance are not visible in the magnitude image of bSSFP, they result in an artifact in the conductivity images (white arrow). On the other hand, conductivity maps obtained via spiral trajectories are free from such distortive artifacts. More importantly, these distortive artifacts arising from the off-resonance can affect a large volume, as depicted in Figure 4.11, for two additional cross sections across the imaging volume.

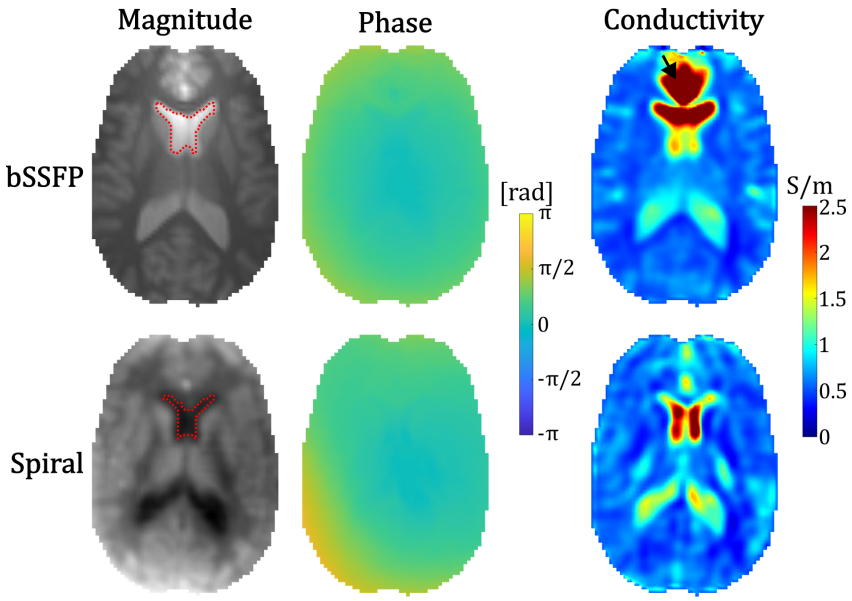

Fig. 4.10: Conductivity maps derived from a healthy volunteer using bSSFP and fully sampled spiral acquisition. The selected ROIs (red dots) are shown overlaid on magnitude images and are used for calculating conductivity values as reported in Table 4.5. The effect of off-resonance, though not clearly visible in the bSSFP magnitude image, can be seen in the conductivity map obtained with the bSSFP (white arrow). In contrast, the conductivity map obtained with the spiral trajectory present no such artifact.

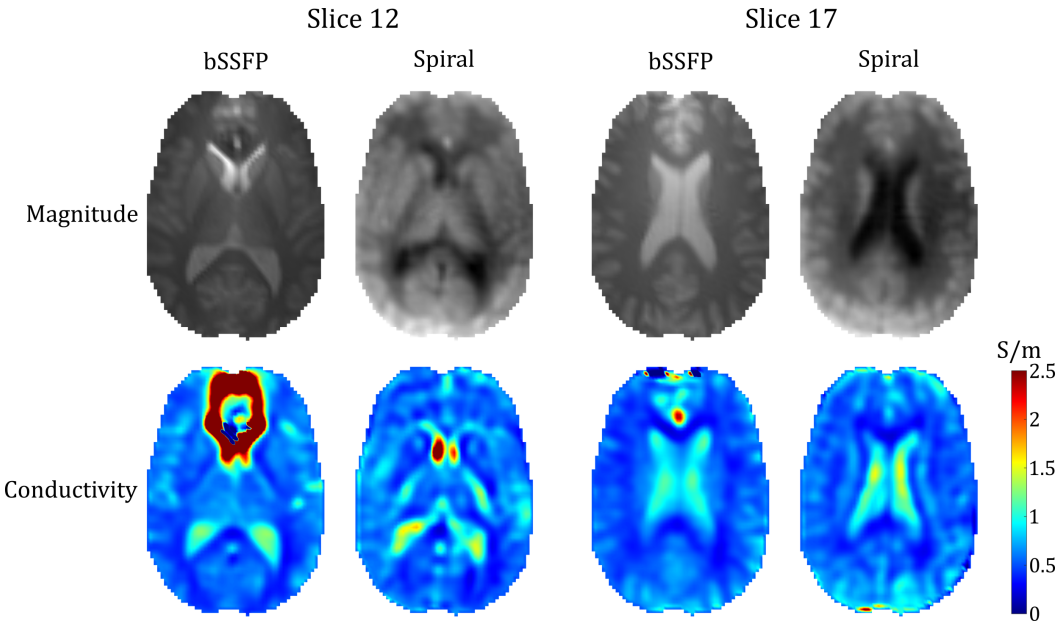

Fig. 4.11: Additional slices of magnitude images and conductivity maps obtained from a healthy volunteer using bSSFP and examplary spiral trajectory (UR/FL/SL = 3/0.5/0.75)

The average conductivity values calculated for the CSF using ROIs (depicted with red dots in Figure 4.10) are listed in Table 4.5. The resulting conductivity values are within the close proximity of the expected value at body temperature, which is 1.794 S/m [71].

Conductivity Values (S/m) for CSF with Different Acquisition Schemes	
Acquisition Type	**Conductivity (mean±sd)**
Fully Sampled	1.142±0.414
UR/FL/SL=2/0.5/0.75	1.613±0.464
UR/FL/SL=3/0.5/0.75	1.969±0.581
UR/FL/SL=4/0.5/0.75	2.083±0.624
UR/FL/SL=2/0.25/0.5	1.499±0.403
UR/FL/SL=3/0.25/0.5	1.728±0.486
UR/FL/SL=4/0.25/0.5	1.889±0.482
bSSFP	2.276±0.886

Tab. 4.5: Conductivity values for CSF with different acquisition schemes. The values are in close proximity with the expected conductivity value at body temperature, which is 1.794 S/m [71]. The effect of banding artifact can be seen here, with the abnormal increase in conductivity values that are obtain with the bSSFP pulse sequence.

5 Discussion

This thesis primarily aims to explore strategies for accelerating the acquisition of complex B_1 data. Currently, literature reports a broad range of acquisition times especially for standard MREPT applications, spanning from slightly more than 5 minutes to more than 8 hours. However, by incorporating an aggressive undersampling scheme with TGV regularization for B_1 magnitude and employing a variable density spiral acquisition for B_1 phase, it is now possible to achieve comprehensive whole-brain coverage in less than 2 minutes.

5.1 Accelerating B_1 Magnitude

The initial approaches of conductivity calculations using the MREPT technique utilized the magnitude and phase of B_1 information together [10]. However, these approaches tend to be slow due to the notoriously slow B_1 magnitude acquisition. To address this, phase-based techniques, which are free from B_1 magnitude, have been proposed [20], [21]. Nevertheless, this alternative is not without its drawbacks: Phase-based conductivity calculations encounter issues, particularly towards the periphery of the imaged object, where a reported 10% error is observed at 3T [20]; this error is likely to increase with higher field strengths [72]. Therefore, a fast technique for acquiring B_1 magnitude is essential to enhance the practicality and efficiency of MREPT applications.

Traditional methods like the Double Angle Method [29], while accurate, are time-consuming due to the requirement of full longitudinal relaxation ($TR \gg 5T_1$). Hafalir, in his cr-MREPT study [61], employed the Double Angle Method and obtained B_1 magnitude maps in 32 minutes. To address this issue and achieve faster results, alternative methods such as Actual Flip-angle Imaging (AFI) [30] and Bloch-Siegert shift-based techniques [31] are employed. However, even these methods have considerable acquisition times. For instance, Katscher used AFI in his standard MREPT study [10], with an acquisition time of around 40 minutes. The challenges are getting worse in multi-channel acquisitions, as demonstrated by Zhang's hybrid

approach [73], where obtaining B_1 magnitude images required 170 minutes for the AFI part only.

Since the effect of B_1 magnitude information is not dominant in conductivity calculations [20], this thesis employs a retrospective heavily undersampled acquisition strategy to demonstrate the feasibility of this strategy for use in MREPT. A 12x4 rectangular pattern placed over the center of k-space was chosen during retrospective undersampling, capitalizing on the absence of high frequencies in B_1 magnitude images. With this scheme, a 3D acquisition can be achieved in less than 30 seconds.

Although a 12x4 rectangular pattern is used in this thesis, different rectangular patterns can easily be implemented. Furthermore, in order to increase incoherence, randomized sampling patterns can also be utilized [68]. In addition, there are many different approaches in order to accelerate B_1 magnitude acquisition via undersampling other than TGV regularization, including jointly reconstructing the images from different transmit coils [74] or using Tikhonov regularization [75].

In addressing the B_1 magnitude component, challenges were encountered, specifically the absence of an applied version for 3D cr-MREPT with the triangular mesh and the presence of the Low Convective Field (LCF) artifact. Hafalir's approach, as outlined in his paper [61], involved the utilization of 2D cr-MREPT with a triangular mesh, neglecting changes in the z-direction. While this proves effective for z-independent phantoms, its applicability to in-vivo imaging becomes problematic. The use of a triangular mesh leads to a high number of nodes, rendering the solution in 3D computationally unsolvable for conventional computers. To overcome this, the interested volume can be segmented into patches, and the solution can be iteratively obtained for each patch, avoiding the challenge of solving for the entire volume in one go. As for addressing the LCF artifact, various methods exist beyond utilizing multi-channel receiver data. These include using multi-transmit coils [63], adopting an inverse problem approach [62], and incorporating dielectric padding [64]. However, it's crucial to note that none of these methods have been tested with in-vivo imaging, underscoring the need for further exploration and validation.

5.2 Accelerating B_1 Phase

In the realm of phase-based techniques for B_1 mapping, a consistent theme emerges: the pursuit of faster acquisition. Katscher, in his study [10], opted for the Actual Flip-angle Imaging (AFI) method, which provided also the phase information but required an additional B_0 map acquisition for B_0 inhomogeneity correction. Even

without this correction, the acqusition time was around 40 minutes. Hafalir, on the other hand, employed a spin echo sequence [61], utilizing two spin echoes with alternating readout directions to eliminate unwanted phase contributions from eddy currents, obtaining B_1 phase images in a total duration of 32 minutes. To expedite acquisition, the balanced steady-state free precession (bSSFP) sequence found widespread use, yet the challenge of banding artifacts necessitated multi-acquisition schemes. Aiming to reduce these artifacts, my previous work [76] utilized two bSSFP acquisitions along with additional acquisitions for B_0 and T_2 mapping, resulting in a total acquisition time of two hours. In order to avoid lengthy B_0 and T_2 maps acquisitions, my following work utilized a multi-acquisition scheme called LORE-GN algorithm [77], which theoretically requires only 3 phase-cycled bSSFP acquisitions. Gavazzi adopted the PLANET method for multi-acquisition scheme, requiring a minimum of 6 different phase-cycled bSSFP acquisitions. In her article [78], Gavazzi employed 8 phase-cycled acquisitions and the acquisition time for B_1 phase map was slightly exceeding 5 minutes. Iyyakkunnel, leveraging configuration theory [79], achieved a total acquisition duration of approximately 10 minutes.

In this thesis, the use of spiral trajectories with various undersampling strategies is investigated for obtaining B_1 phase for conductivity imaging. Spiral trajectories were a natural candidate for this work due to their center-out sampling strategy, which efficiently covers low k-space frequencies. By employing undersampling with spiral trajectories, the total acquisition time was substantially reduced without compromising image quality, as demonstrated in both phantom and volunteer experiments. With the chosen sampling scheme of UR/FL/SL=3/0.5/0.75, the conductivity values obtained in the phantom experiments (0.381 S/m for the background and 0.887 S/m for the structures) were in good agreement with the expected values (0.35 S/m for the background and 1.04 S/m for the structures). The CSF conductivity values obtained in the in vivo experiments (1.969 S/m) are close to the expected value at body temperature, which is 1.794 S/m [71]. Overall, the results suggest that spiral trajectories with undersampling are a promising approach for fast conductivity imaging, enabling the acquisition of whole brain coverage in less than a minute.

The use of spiral trajectories with undersampling strategies offers significant advantages in terms of acquisition time. The center-out sampling strategy implemented in this study prioritizes low k-space frequencies, thus allowing the acquisition of low spatial frequency information at a high temporal resolution. This property is particularly useful for conductivity imaging, as the phase data from which conductivity is calculated do not contain high frequency components. Furthermore, spiral acquisitions excel in covering k-space rapidly, particularly with long readouts. This rapid k-space coverage sets spirals apart from their Cartesian counterparts, further

enhancing their suitability for applications that demand swift data acquisition. As a result, a single slice with multiple averages can be obtained in less than a second, and whole brain imaging can be conducted in less than a minute, making spiral acquisitions with undersampling schemes particularly well-suited for clinical applications.

It is crucial to highlight that Cartesian methods, which focus on the k-space center, can play a vital role in expediting B_1 phase acquisition. Traditional approaches such as SENSE [43] and GRAPPA [44] contribute to hastening data collection with Cartesian trajectories, addressing the need for increased acquisition speed. Additionally, their non-Cartesian counterparts, like Conjugate Gradient SENSE (CG SENSE) [80] or spiral GRAPPA [81], can also be leveraged for this purpose.

Spiral imaging is known for its low minimum TE, allowing for imaging of challenging tissue types like the lung [82] or heart [83]. Alongside with the acquisition speed advantages, spiral imaging has already made real-time phase-contrast imaging feasible [84]. The implementation of these techniques may pave the way for real-time MREPT imaging in the future.

Compared to other commonly used pulse sequences in MREPT, such as bSSFP, spiral imaging offers distinct advantages in terms of artifact reduction. bSSFP images are particularly vulnerable to off-resonance, which can substantially distort conductivity images as demonstrated in Figure 4.10. This phenomenon arises because the observed phase is dependent on the off-resonance [76]. In particular, approximately π-radian phase differences in the vicinity of banding artifacts are further amplified by the Laplacian operation used in the conductivity calculations. In contrast, spiral imaging exhibits less coherent aliasing artifacts compared to Cartesian trajectories, especially when undersampling is utilized [85]. Additionally, spiral imaging is inherently oversampled at the k-space center, which makes it more robust against motion artifacts [85].

The expected [67] and actual conductivity values in the phantom experiments are in close agreement, however differences exist, which are stemming from two main source of errors. First, discrepancy between expected and actual conductivity values is higher for the structures than for the background. This could be due to either the limitations in the assumptions used for phase-based conductivity reconstructions, [72] such as transceiver phase assumption and low B_1 magnitude gradient assumption, or simply the smoothing effect introduced by applying a Gaussian filter to the phase data. Second, halo artifacts in both phantom and in vivo images were observed. Main causes suspected of leading to this well-known artifact in spiral imaging are static off-resonance and concomitant fields, resulting in blurring

or ringing in the image, as well as gradients imperfections, causing artifacts near the edge of the imaged object [53]. While these artifacts can be mitigated with the utilization of undersampling, there are additional approaches that can be employed to further eliminate these unwanted effects, including calculating the delays of the gradients [54], correction of B_0 eddy currents [55], or even simultaneous correction of off-resonance, trajectory errors, and concomitant field effects together [56]. These approaches can be integrated together with undersampling strategies to further suppress these artifacts.

The utilization of spiral trajectories in MREPT presents a promising prospect for clinical applications. MREPT has been previously applied in various clinical scenarios, such as brain tumours [86], ischemia [23], and hemorrhage cases [23]. In these scenarios, the phrase "time is brain" rings particularly true, making fast acquisition techniques like spiral imaging crucial for the successful implementation of MREPT. The rapid acquisition provided by spiral imaging can enable clinicians to obtain high-quality conductivity images within clinically feasible timescales, making it an attractive option for future clinical studies. However, further validation is required to establish the clinical utility of spiral MREPT and its superiority over other imaging techniques in various clinical scenarios.

Acquisition of B_1 phase can benefit from the application of machine learning techniques, offering a potential avenue for further enhancing image quality and acceleration. Several noteworthy works in the field have already been published. In 2019, Mandija introduced Deep Learning Electrical Properties Tomography (DL-EPT) [87], employing Conditional Generative Adversarial Networks for conductivity reconstruction. Building on this, Gavazzi utilized DL-EPT for in-vivo pelvis conductivity in 2020 [88]. The following year, in 2021, Jung leveraged deep learning to denoise B_1 phase data [89], demonstrating superior performance compared to Gaussian and Savitzky-Golay filtering methods. The latest contribution came in 2023, as Jung proposed another conductivity reconstruction technique utilizing artificial neural networks [90]. Through a comprehensive comparison with various available reconstruction techniques, this data-driven approach showcased superior accuracy and image quality. Combining the method presented in this work with machine learning techniques would be interesting to explore in future studies.

6 Conclusion and Outlook

Conductivity serves as a valuable diagnostic tool for a range of diseases, including tumors, inflammation, and edema. Additionally, it finds application in treatments like transcranial magnetic stimulation and RF ablation. Several MRI-based methods have been developed for obtaining conductivity values [10], [15]–[18]. A recent advancement in this field is Magnetic Resonance Electrical Properties Tomography (MREPT) [10], which derives conductivity through complex B_1 mapping. Notably, this technique is non-invasive and doesn't require additional hardware. However, the main obstacle lies in the time-consuming nature of the process. Initial experiments took approximately 40-60 minutes [10], [61], and with multi-channel schemes, this duration could extend to multiple hours [73]. In response to this challenge, the central objective of this thesis is to significantly reduce the acquisition time for B_1 phase and magnitude acquisitions, thereby enabling the clinical applicability of MREPT.

To expedite the acquisition of B_1 magnitude, an undersampling strategy coupled with Total Generalized Variation (TGV) regularization is employed. Specifically, a 12x4 rectangular block at the center of the k-space is retrospectively chosen, enabling an acceleration of up to 85 times. Phantom experiments using two distinct reconstruction techniques revealed no discernible difference in conductivity values between fully sampled and retrospectively undersampled B_1 magnitude. As a result, an accurate 3D B_1 magnitude acquisition can be accomplished in a remarkably short time-frame of just 30 seconds.

To accelerate the B_1 phase acquisition, a strategy involving variable density spiral trajectories and SPIRiT parallel imaging reconstruction is employed. Both phantom and in vivo experiments demonstrated the successful acquisition of conductivity with meticulous undersampling parameter selection. The chosen undersampling scheme allowed for the B_1 phase acquisition of a single slice with multiple averages in less than a second, while achieving whole-brain coverage within 60 seconds.

In summary, this work effectively reduces the acquisition time for conductivity imaging through MRI. The methodologies introduced herein hold promise as valuable tools for the clinical integration of MRI-based conductivity imaging techniques.

List of Figures

2.1 Direction of nuclear magnetic moment vectors for two different nuclei, $^{1}\mathrm{H}$ ($I = 1/2$) and $^{23}\mathrm{Na}$ ($I = 3/2$). 7
2.2 Zeeman spliting for $^{1}\mathrm{H}$ ($I = 1/2$) and $^{23}\mathrm{Na}$ ($I = 3/2$). 7
2.3 Exponential growth of the longitudinal component and exponential decay of the transversal component after an initial 90° pulse. 13
2.4 Sampling in the k-space domain and its corresponding replication in the image domain. 18
2.5 A standard pulse sequence diagram and its corresponding k-space coverage. 19
2.6 Different central k-space data masks and their corresponding images. . 20
2.7 Different peripheral k-space data masks and their corresponding images. 21
2.8 A GRE pulse sequence diagram. 22
2.9 T_2* decay, accelerated decay due to the introduction of gradients and obtained MRI signal. 22
2.10 A SE pulse sequence diagram. 23
2.11 A bSSFP pulse sequence diagram. 24
2.12 bSSFP signal profiles with magnitude and phase for white matter and CSF. 25
2.13 Pulse sequence diagrams for EPI, radial, and spiral acquisitions. 28
2.14 Different sampling patterns for MRI acquisitions. 28
2.15 The representation of the effective B_1 field in the Bloch-Siegert shift based method. 35

3.1 Pulse sequence diagram for Bloch-Siegert shift based B_1 mapping method. 40
3.2 k-space sampling patterns. 40
3.3 Constructed phantom that is used in the conductivity experiments. . . 41
3.4 User interface of the spiral trajectory based pulse sequence. 43
3.5 k-space trajectories of different sampling schemes 45

4.1 For two different slices, magnitude and phase of the bSSFP image. . . . 47

4.2 For the phantom experiment, retrospectively undersampled B_1 magnitude images, fully sampled B_1 magnitude images and their ratios for two different slices. 48
4.3 Conductivity maps, obtained with retrospectively undersampled B_1 magnitude images and fully sampled B_1 magnitude imagesvia standard MREPT method for two different slices. 49
4.4 The conductivity maps, obtained with retrospectively undersampled B_1 magnitude images and fully sampled B_1 magnitude images via cr-MREPT method for two different slices. 49
4.5 Fully sampled phase and phase differences of each undersampled scheme with respect to fully sampled case. 51
4.6 Conductivity images obtained through the phase-based cr-MREPT technique in phantom measurements. 51
4.7 Conductivity differences of different undersampling schemes with respect to the fully sampled acquisition. 52
4.8 Conductivity images obtained with varying numbers of averages. . . . 53
4.9 Conductivity maps derived from a healthy volunteer using various sampling schemes. 54
4.10 Conductivity maps derived from a healthy volunteer using bSSFP and fully sampled spiral acquisition. 55
4.11 Additional slices of magnitude images and conductivity maps obtained from a healthy volunteer using bSSFP and examplary spiral trajectory (UR/FL/SL = 3/0.5/0.75) 55

List of Tables

2.1 List of selected nuclei, their spin quantum number (I), gyromagnetic ratios (γ), and abundance in human body. 6
2.2 List of relaxation times for various tissue types at 3T. 13
2.3 Permittivity, ε, and conductivity, σ of various tissues in human body at 127 MHz [58]. 30

3.1 Sequence parameters for in vivo (phantom) experiments. 45

4.1 Mean and standard deviation of conductivity values with different sampling patterns and reconstruction techniques for the 16th slice. . . 50
4.2 Mean and standard deviation of conductivity values with different sampling patterns and reconstruction techniques for the 8th slice. . . . 50
4.3 Mean and standard deviation of conductivity values obtained from phantom experiments using different sampling schemes. 52
4.4 Mean and standard deviation of conductivity values with different number of averages. 53
4.5 Conductivity values for CSF with different acquisition schemes. 56

Curriculum Vitae

Date of Birth: 27/05/1993
Place of Birth: Malatya, Turkey
Citizenship: Turkish
E-mail: safa.oezdemir@medma.uni-heidelberg.de
Date of Issue: July 15, 2024

EDUCATION

Heidelberg University, Heidelberg, Germany
Dr. sc. hum. in Medical Faculty Mannheim — Sept. 2020 -
Bilkent University, Ankara, Turkey
M.Sc. in Electrical and Electronics Engineering
GPA: 3.16/4.00 — Sept. 2015 - Sept. 2018
B.S. in Electrical and Electronics Engineering
GPA: 3.26/4.00 — Sept. 2010 - June 2015

INDUSTRIAL & ACADEMIC EXPERIENCE

Research Assistant
Department of Computer Assisted Clinical Medicine
University of Heidelberg, Germany — March 2020 - Present
Department of Electrical and Electronics Engineering
Bilkent University, Ankara, Turkey — Fall 2015 - Spring 2019
Teaching Assistant
Department of Computer Assisted Clinical Medicine
University of Heidelberg, Germany — March 2020 - Present
Department of Electrical and Electronics Engineering
Bilkent University, Ankara, Turkey — Fall 2015 - Spring 2019

AWARDS & HONORS

- **1st Place Award in ETP Category** in Electro-Magnetic Tissue Properties Study Group Meeting, In Proceedings of the 31st Annual Meeting of ISMRM, Toronto, Canada, 2023
- **Bilkent University Full Scholarship** for M.Sc. degree in EEE Department.
- **Bilkent University Honor** student during undergraduate studies.
- **Industrial Project Grant** awarded by The Scientific and Technological Research Council of Turkey (TUBITAK), in 2014.
- **Research Excellence Award** during undergraduate studies, in 2014.
- **Bilkent University Comprehensive Scholarship** for B.S. degree in EEE Department.
- **27th in the National University Entrance Examination** among more than 1M candidates, 2010.

List of Publications

JOURNAL PAPERS

- **Ozdemir S.**, Ilicak E., Zapp J., Schad L.R., and Zöllner F.G., "Feasibility of undersampled spiral trajectories in MREPT for fast conductivity imaging," *Magnetic Resonance in Medicine*, 2023.
  Accepted on 13 November, 2023

- Ilicak E., Thater G., **Ozdemir S.**, Zapp J., Schad L.R., Schoenberg S.O., Zöllner F.G., and Weis M., "Functional lung imaging of 2-year-old children after congenital diaphragmatic hernia repair using dynamic mode decomposition MRI," *European Radiology*, 2023.
  https://doi.org/10.1007/s00330-023-10335-6

- Ilicak E., **Ozdemir S.**, Zapp J., Schad L.R., and Zöllner F.G., "Dynamic mode decomposition of dynamic MRI for assessment of pulmonary ventilation and perfusion," *Magnetic Resonance in Medicine*, vol. 90, no. 2, pp. 761-769, 2023.
  https://doi.org/10.1002/mrm.29656

- Adlung A., Licht C., Reichert S., **Ozdemir S.**, Mohamed S.A., Samartzi M., Fatar M., Gass A., Prost E.N., and Schad L.R., "Quantification of tissue sodium concentration in the ischemic stroke: A comparison between external and internal references for 23Na MRI," *Journal of Neuroscience Methods*, vol. 382, p. 109721, 2022.
  https://doi.org/10.1016/j.jneumeth.2022.109721

- Ilicak E., **Ozdemir S.**, Schad L.R., Weis M., Schoenberg S.O., Zöllner F.G., and Zapp J., "Phase-cycled balanced SSFP imaging for non-contrast-enhanced functional lung imaging," *Magnetic Resonance in Medicine*, vol. 88, no. 4, pp. 1764-1774, 2022.
  https://doi.org/10.1002/mrm.29302

- **Ozdemir S.** and Ider Y.Z., "bSSFP Phase Correction and its use in Magnetic Resonance Electrical Properties Tomography," *Magnetic Resonance in Medicine*, vol. 81, no. 2, pp. 934-946, 2018.
  https://doi.org/10.1002/mrm.27446

CONFERENCE PAPERS

- **Ozdemir S.**, Ilicak E., Schad L.R., Zöllner F.G., "Investigating Variable Density Sampling Patterns in Spiral Trajectories for use in MREPT", In: *Proceedings of the 31st Annual Meeting of ISMRM*, 5164, Toronto, Canada, 2023

- Ilicak E., **Ozdemir S.**, Zapp J., Schad L.R., Zöllner F.G., "Using Dynamic Mode Decomposition for Functional Lung Imaging", In: *Proceedings of the 31st Annual Meeting of ISMRM*, 4671, Toronto, Canada, 2023

- **Ozdemir S.**, Ilicak E., Schad L.R., Zöllner F.G., "Investigating Spiral Trajectories for Sub-second Conductivity Imaging", In: *Proceedings of the 30th Annual Meeting of ISMRM*, 2915, London, United Kingdom, 2022

- Ilicak E., **Ozdemir S.**, Schad L.R., Zapp J., Zöllner F.G., "Improving reconstruction quality in non-contrast-enhanced functional lung imaging via LORAKS", In: *Proceedings of the 30th Annual Meeting of ISMRM*, 1478, London, United Kingdom, 2022

- **Ozdemir S.**, Ilicak E., Stutz C., Berger M., Zapp J., Schad L.R., Ider Y.Z., Zöllner F.G., "Fast 3D Undersampled Bloch-Siegert based B1+ Mapping for use in MREPT", In: *Proceedings of the 29th Annual Meeting of ISMRM*, 3780, Vancouver, Canada, 2021

- Ilicak E., Zapp J., **Ozdemir S.**, Schad L.R., Zöllner F.G., "Phase-Cycled Balanced Steady-State Free Precession Imaging for Functional Lung Imaging at 1.5 and 3 Tesla", In: *Proceedings of the 29th Annual Meeting of ISMRM*, 3230, Vancouver, Canada, 2021

- **Ozdemir S.** and Ider Y.Z., "Estimation of transceive phase via LORE-GN algorithm and its use in MREPT", In: *Proceedings of the 27th Annual Meeting of ISMRM*, 5053, Montreal, Canada, 2019

- **Ozdemir S.** and Ider Y.Z., "bSSFP Phase Correction and its use in MREPT", In: *Proceedings of the 26th Annual Meeting of ISMRM*, 5089, Paris, France, 2018

- Ertan K., Taraghinia S., Takmaz A., Dogan S.E., **Ozdemir S.**, Atalar E., "Spatiotemporal Magnetic Field Monitoring with Hall Effect Sensors" *In Proceedings of the 25th Annual Meeting of ISMRM*, 3910, Honolulu, USA, 2017.

- Ariyurek C., **Ozdemir S.**, Ergun A.S., Ider Y.Z., Atalar E., "Experimental Validation of High Shear Wave Displacement at Mode Frequencies in MR Elastography", In: *Proceedings of the 24th Annual Meeting of ISMRM*, 1960, Singapore, Singapore, 2016.
- Ariyurek C., Ider Y.Z., Gurler N., **Ozdemir S.**, Emek A., Ergun A.S., Atalar E., "Modes of Shear Waves in Brain MR Elastography", In: *Proceedings of the 22nd Annual Meeting of ISMRM*, 4270, Milan, Italy, 2014.

Bibliography

[1] C. Gabriel, S. Gabriel, and E. Corthout, "The dielectric properties of biological tissues: I. literature survey," *Physics in Medicine and Biology*, vol. 41, no. 11, pp. 2231–2249, 1996.

[2] S. Gabriel, R. Lau, and C. Gabriel, "The dielectric properties of biological tissues: II. measurements in the frequency range 10 hz to 20 ghz," *Physics in Medicine and Biology*, vol. 41, no. 11, pp. 2251–2269, 1996.

[3] A. Surowiec, S. Stuchly, J. Barr, *et al.*, "Dielectric properties of breast carcinoma and the surrounding tissues," *IEEE Transactions on Biomedical Engineering*, vol. 35, no. 4, pp. 257–263, 1988.

[4] D. Haemmerich, S. Staelin, J. Tsai, *et al.*, "In vivo electrical conductivity of hepatic tumours," *Physiological Measurement*, vol. 24, no. 2, pp. 251–260, 2003.

[5] R. Smallwood, A. Keshtkar, B. Wilkinson, *et al.*, "Electrical impedance spectroscopy (EIS) in the urinary bladder: The effect of inflammation and edema on identification of malignancy," *IEEE Transactions on Medical Imaging*, vol. 21, no. 6, pp. 708–710, 2002.

[6] L. Liu, W. Dong, X. Ji, *et al.*, "A new method of noninvasive brain-edema monitoring in stroke: Cerebral electrical impedance measurement," *Neurological Research*, vol. 28, no. 1, pp. 31–37, 2006.

[7] M. George, S. Lisanby, and H. Sackeim, "Transcranial magnetic stimulation," *Archives of General Psychiatry*, vol. 56, no. 4, p. 300, 1999.

[8] A. Roy, B. Baxter, and B. He, "High-definition transcranial direct current stimulation induces both acute and persistent changes in broadband cortical synchronization: A simultaneous tDCS–EEG study," *IEEE Transactions on Biomedical Engineering*, vol. 61, no. 7, pp. 1967–1978, 2014.

[9] C. Pappone, S. Rosanio, G. Oreto, *et al.*, "Circumferential radiofrequency ablation of pulmonary vein ostia," *Circulation*, vol. 102, no. 21, pp. 2619–2628, 2000.

[10] U. Katscher, T. Voigt, C. Findeklee, *et al.*, "Determination of electric conductivity and local SAR via B1 mapping," *IEEE Transactions on Medical Imaging*, vol. 28, no. 9, pp. 1365–1374, 2009.

[11] V. Mishra, H. Bouayad, A. Schned, *et al.*, "A real-time electrical impedance sensing biopsy needle," *IEEE Transactions on Biomedical Engineering*, vol. 59, no. 12, pp. 3327–3336, 2012.

[12] D. Barber and B. Brown, "Applied potential tomography," *Journal of Physics E: Scientific Instruments*, vol. 17, no. 9, pp. 723–733, 1984.

[13] H. Griffiths, "Magnetic induction tomography," *Measurement Science and Technology*, vol. 12, no. 8, pp. 1126–1131, 2001.

[14] G. Scott, M. Joy, R. Armstrong, *et al.*, "Measurement of nonuniform current density by magnetic resonance," *IEEE Transactions on Medical Imaging*, vol. 10, no. 3, pp. 362–374, 1991.

[15] J. Seo, J. Yoon, E. Woo, *et al.*, "Reconstruction of conductivity and current density images using only one component of magnetic field measurements," *IEEE Transactions on Biomedical Engineering*, vol. 50, no. 9, pp. 1121–1124, 2003.

[16] Y. Ider and S. Onart, "Algebraic reconstruction for 3D magnetic resonance–electrical impedance tomography (MREIT) using one component of magnetic flux density," *Physiological Measurement*, vol. 25, no. 1, pp. 281–294, 2004.

[17] L. Özparlak and Y. İder, "Induced current magnetic resonance–electrical impedance tomography," *Physiological Measurement*, vol. 26, no. 2, pp. 289–305, 2005.

[18] E. Haacke, L. Petropoulos, E. Nilges, *et al.*, "Extraction of conductivity and permittivity using magnetic resonance imaging," *Physics in Medicine and Biology*, vol. 36, no. 6, pp. 723–734, 1991.

[19] H. Wen, "Noninvasive quantitative mapping of conductivity and dielectric distributions using RF wave propagation effects in high-field MRI," in *Proceedings of SPIE Vol. 5030: Medical Imaging 2003: Physics of Medical Imaging*, 2003, pp. 471–477.

[20] T. Voigt, U. Katscher, and O. Doessel, "Quantitative conductivity and permittivity imaging of the human brain using electric properties tomography," *Magnetic Resonance in Medicine*, vol. 66, no. 2, pp. 456–466, 2011.

[21] N. Gurler and Y. Ider, "Gradient-based electrical conductivity imaging using MR phase," *Magnetic Resonance in Medicine*, vol. 77, no. 1, pp. 137–150, 2016.

[22] K. Tha, U. Katscher, S. Yamaguchi, *et al.*, "Noninvasive electrical conductivity measurement by MRI: A test of its validity and the electrical conductivity characteristics of glioma," *European Radiology*, vol. 28, no. 1, pp. 348–355, 2017.

[23] N. Gurler, O. Oran, H. Keklikoglu, *et al.*, "Application of generalized phase based electrical conductivity imaging in the subacute stage of hemorrhagic and ischemic strokes," in *Proceedings of the 24th Annual Meeting of ISMRM*, 2994, Singapore, Singapore, 2016.

[24] J. Shin, M. Kim, J. Lee, *et al.*, "Initial study on in vivo conductivity mapping of breast cancer using MRI," *Journal of Magnetic Resonance Imaging*, vol. 42, no. 2, pp. 371–378, 2014.

[25] D. Kim, N. Choi, S. Gho, *et al.*, "Simultaneous imaging of in vivo conductivity and susceptibility," *Magnetic Resonance in Medicine*, vol. 71, no. 3, pp. 1144–1150, 2013.

[26] S. Gho, J. Shin, M. Kim, *et al.*, "Simultaneous quantitative mapping of conductivity and susceptibility using a double-echo ultrashort echo time sequence: Example using a hematoma evolution study," *Magnetic Resonance in Medicine*, vol. 76, no. 1, pp. 214–221, 2015.

[27] S. Lee, S. Bulumulla, F. Wiesinger, *et al.*, "Tissue electrical property mapping from zero echo-time magnetic resonance imaging," *IEEE Transactions on Medical Imaging*, vol. 34, no. 2, pp. 541–550, 2015.

[28] C. Stehning, T. Voigt, and U. Katscher, "Real time conductivity mapping using balanced SSFP and phase based reconstruction," in *Proceedings of the 19th Annual Meeting of ISMRM*, 0128, Montreal, Canada, 2011.

[29] R. Stollberger and P. Wach, "Imaging of the active B1 field in vivo," *Magnetic Resonance in Medicine*, vol. 35, no. 2, pp. 246–251, 1996.

[30] V. Yarnykh, "Actual flip-angle imaging in the pulsed steady state: A method for rapid three-dimensional mapping of the transmitted radiofrequency field," *Magnetic Resonance in Medicine*, vol. 57, no. 1, pp. 192–200, 2006.

[31] L. Sacolick, F. Wiesinger, I. Hancu, *et al.*, "B1 mapping by Bloch-Siegert shift," *Magnetic Resonance in Medicine*, vol. 63, no. 5, pp. 1315–1322, 2010.

[32] D. Hoult and R. Richards, "The signal-to-noise ratio of the nuclear magnetic resonance experiment," *Journal of Magnetic Resonance*, vol. 24, no. 1, pp. 71–85, 1976.

[33] M. Bernstein, K. King, and X. Zhou, *Handbook of MRI Pulse Sequences*. Elsevier Science, 2004.

[34] J. P. Reilly, "Peripheral nerve stimulation by induced electric currents: Exposure to time-varying magnetic fields," *Medical & Biological Engineering & Computing*, vol. 27, no. 2, pp. 101–110, 1989.

[35] D. Schaefer, J. Bourland, and J. Nyenhuis, "Review of patient safety in time-varying gradient fields," *Journal of Magnetic Resonance Imaging*, vol. 12, no. 1, pp. 20–29, 2000.

[36] D. Nishimura, *Principles of Magnetic Resonance Imaging*. Stanford University, 1996.

[37] E. Hahn, "Spin echoes," *Physical Review*, vol. 80, no. 4, pp. 580–594, 1950.

[38] H. Carr and E. Purcell, "Effects of diffusion on free precession in nuclear magnetic resonance experiments," *Physical Review*, vol. 94, no. 3, pp. 630–638, 1954.

[39] H. Carr, "Steady-state free precession in nuclear magnetic resonance," *Physical Review*, vol. 112, no. 5, pp. 1693–1701, 1958.

[40] M. Lauzon and R. Frayne, "Analytical characterization of RF phase-cycled balanced steady-state free precession," *Concepts in Magnetic Resonance Part A*, vol. 34A, no. 3, pp. 133–143, 2009.

[41] M. Björk, R. R. Ingle, E. Gudmundson, *et al.*, "Parameter estimation approach to banding artifact reduction in balanced steady-state free precession," *Magnetic Resonance in Medicine*, vol. 72, no. 3, pp. 880–892, 2013.

[42] O. Bieri and K. Scheffler, "Fundamentals of balanced steady state free precession MRI," *Journal of Magnetic Resonance Imaging*, vol. 38, no. 1, pp. 2–11, 2013.

[43] K. Pruessmann, M. Weiger, M. Scheidegger, *et al.*, "SENSE: Sensitivity encoding for fast MRI," *Magnetic Resonance in Medicine*, vol. 42, no. 5, pp. 952–962, 1999.

[44] M. Griswold, P. Jakob, R. Heidemann, *et al.*, "Generalized autocalibrating partially parallel acquisitions (GRAPPA)," *Magnetic Resonance in Medicine*, vol. 47, no. 6, pp. 1202–1210, 2002.

[45] J. Hamilton, D. Franson, and N. Seiberlich, "Recent advances in parallel imaging for MRI," *Progress in Nuclear Magnetic Resonance Spectroscopy*, vol. 101, pp. 71–95, 2017.

[46] M. Lustig and J. Pauly, "SPIRiT: Iterative self-consistent parallel imaging reconstruction from arbitrary k-space," *Magnetic Resonance in Medicine*, vol. 64, no. 2, pp. 457–471, 2010.

[47] P. Jezzard and R. Balaban, "Correction for geometric distortion in echo planar images from B0 field variations," *Magnetic Resonance in Medicine*, vol. 34, no. 1, pp. 65–73, 1995.

[48] S. Reeder, E. Atalar, B. Bolster, *et al.*, "Quantification and reduction of ghosting artifacts in interleaved echo-planar imaging," *Magnetic Resonance in Medicine*, vol. 38, no. 3, pp. 429–439, 1997.

[49] H. Ward, S. Riederer, and C. Jack, "Real-time autoshimming for echo planar timecourse imaging," *Magnetic Resonance in Medicine*, vol. 48, no. 5, pp. 771–780, 2002.

[50] J. Pipe, "Motion correction with propeller MRI: Application to head motion and free-breathing cardiac imaging," *Magnetic Resonance in Medicine*, vol. 42, no. 5, pp. 963–969, 1999.

[51] L. Feng, R. Grimm, K. Block, *et al.*, "Golden-angle radial sparse parallel MRI: Combination of compressed sensing, parallel imaging, and golden-angle radial sampling for fast and flexible dynamic volumetric MRI," *Magnetic Resonance in Medicine*, vol. 72, no. 3, pp. 707–717, 2013.

[52] Y. Xue, J. Yu, H. Kang, *et al.*, "Automatic coil selection for streak artifact reduction in radial MRI," *Magnetic Resonance in Medicine*, vol. 67, no. 2, pp. 470–476, 2011.

[53] K. Block and J. Frahm, "Spiral imaging: A critical appraisal," *Journal of Magnetic Resonance Imaging*, vol. 21, no. 6, pp. 657–668, 2005.

[54] R. Robison, A. Devaraj, and J. Pipe, "Fast, simple gradient delay estimation for spiral MRI," *Magnetic Resonance in Medicine*, vol. 63, no. 6, pp. 1683–1690, 2010.

[55] R. Robison, Z. Li, D. Wang, *et al.*, "Correction of B0 eddy current effects in spiral mri," *Magnetic Resonance in Medicine*, vol. 81, no. 4, pp. 2501–2513, 2018.

[56] N. Lee, R. Ramasawmy, Y. Lim, *et al.*, "MaxGIRF: Image reconstruction incorporating concomitant field and gradient impulse response function effects," *Magnetic Resonance in Medicine*, vol. 88, no. 2, pp. 691–710, 2022.

[57] R. J. Halter, A. Schned, J. Heaney, *et al.*, "Electrical properties of prostatic tissues: I. single frequency admittivity properties," *Journal of Urology*, vol. 182, no. 4, pp. 1600–1607, 2009.

[58] *Dielectric properties it'is foundation*, https://itis.swiss/virtual-population/tissue-properties/database/dielectric-properties/, Accessed: 2023-11-14.

[59] J. Liu, Y. Wang, U. Katscher, *et al.*, "Electrical properties tomography based on B1 maps in MRI: Principles, applications, and challenges," *IEEE Transactions on Biomedical Engineering*, vol. 64, no. 11, pp. 2515–2530, 2017.

[60] U. Katscher, D. Kim, and J. Seo, "Recent progress and future challenges in MR electric properties tomography," *Computational and Mathematical Methods in Medicine*, vol. 2013, pp. 1–11, 2013.

[61] F. Hafalir, O. Oran, N. Gurler, *et al.*, "Convection-reaction equation based magnetic resonance electrical properties tomography (cr-MREPT)," *IEEE Transactions on Medical Imaging*, vol. 33, no. 3, pp. 777–793, 2014.

[62] Y. Ider and C. Boga, "Inverse problem approach to cr-MREPT," in *Proceedings of the 27th Annual Meeting of ISMRM*, 5052, Montreal, Canada, 2019.

[63] G. Ariturk and Y. Ider, "Optimal multichannel transmission for improved cr-MREPT," *Physics in Medicine & Biology*, vol. 63, no. 4, p. 045 001, 2018.

[64] G. Yildiz and Y. Ider, "Use of dielectric padding to eliminate low convective field artifact in cr-MREPT conductivity images," *Magnetic Resonance in Medicine*, vol. 81, no. 5, pp. 3168–3184, 2019.

[65] G. Yildiz and Y. Ider, "LCF artifact elimination in cr-MREPT using phased-array receive coil," in *Proceedings of the 26th Annual Meeting of ISMRM*, 5093, Paris, France, 2018.

[66] S. Ozdemir, E. Ilicak, M. Stutz, *et al.*, "Fast 3D undersampled Bloch-Siegert based B1+ mapping for use in MREPT," in *Proceedings of the 29th Annual Meeting of ISMRM*, 3780, Singapore, Singapore, 2021.

[67] A. Stogryn, "Equations for calculating the dielectric constant of saline water," *IEEE Transactions on Microwave Theory and Techniques*, vol. 19, no. 8, pp. 733–736, 1971.

[68] A. Lesch, M. Schlöegl, M. Holler, *et al.*, "Ultrafast 3D Bloch–Siegert B1+-mapping using variational modeling," *Magnetic Resonance in Medicine*, vol. 81, no. 2, pp. 881–892, 2018.

[69] S. Ozdemir, E. Ilicak, J. Zapp, *et al.*, "Feasibility of undersampled spiral trajectories in MREPT for fast conductivity imaging," *Magnetic Resonance in Medicine*,

[70] J. Pipe and N. Zwart, "Spiral trajectory design: A flexible numerical algorithm and base analytical equations," *Magnetic Resonance in Medicine*, vol. 71, no. 1, pp. 278–285, 2013.

[71] S. Baumann, D. Wozny, S. Kelly, *et al.*, "The electrical conductivity of human cerebrospinal fluid at body temperature," *IEEE Transactions on Biomedical Engineering*, vol. 44, no. 3, pp. 220–223, 1997.

[72] A. van Lier, D. Brunner, K. Pruessmann, *et al.*, "B1 phase mapping at 7T and its application for in vivo electrical conductivity mapping," *Magnetic Resonance in Medicine*, vol. 67, no. 2, pp. 552–561, 2011.

[73] X. Zhang, P. de Moortele, S. Schmitter, *et al.*, "Complex B1 mapping and electrical properties imaging of the human brain using a 16-channel transceiver coil at 7T," *Magnetic Resonance in Medicine*, vol. 69, no. 5, pp. 1285–1296, 2012.

[74] A. Sharma, S. Tadanki, M. Jankiewicz, *et al.*, "Highly-accelerated Bloch-Siegert |B1+| mapping using joint autocalibrated parallel image reconstruction," *Magnetic Resonance in Medicine*, vol. 71, no. 4, pp. 1470–1477, 2013.

[75] F. Zhao, J. Fessler, S. Wright, *et al.*, "Regularized estimation of magnitude and phase of multi-coil B1 field via Bloch–Siegert B1 mapping and coil combination optimizations," *IEEE Transactions on Medical Imaging*, vol. 33, no. 10, pp. 2020–2030, 2014.

[76] S. Ozdemir and Y. Ider, "bSSFP phase correction and its use in magnetic resonance electrical properties tomography," *Magnetic Resonance in Medicine*, vol. 81, no. 2, pp. 934–946, Feb. 2019.

[77] S. Ozdemir and Y. Ider, "Estimation of transceive phase via LORE-GN algorithm and its use in MREPT," in *Proceedings of the 27th Annual Meeting of ISMRM*, 5053, Montreal, Canada, 2019.

[78] S. Gavazzi, Y. Shcherbakova, L. Bartels, *et al.*, "Transceive phase mapping using the PLANET method and its application for conductivity mapping in the brain," *Magnetic Resonance in Medicine*, vol. 83, no. 2, pp. 590–607, 2019.

[79] S. Iyyakkunnel, J. Schäper, and O. Bieri, "Configuration-based electrical properties tomography," *Magnetic Resonance in Medicine*, vol. 85, no. 4, pp. 1855–1864, 2020.

[80] K. Pruessmann, M. Weiger, P. Börnert, *et al.*, "Advances in sensitivity encoding with arbitrary k-space trajectories," *Magnetic Resonance in Medicine*, vol. 46, no. 4, pp. 638–651, 2001.

[81] N. Seiberlich, G. Lee, P. Ehses, *et al.*, "Improved temporal resolution in cardiac imaging using through-time spiral GRAPPA," *Magnetic Resonance in Medicine*, vol. 66, no. 6, pp. 1682–1688, 2011.

[82] A. Javed, R. Ramasawmy, K. O'Brien, *et al.*, "Self-gated 3D stack-of-spirals ute pulmonary imaging at 0.55T," *Magnetic Resonance in Medicine*, vol. 87, no. 4, pp. 1784–1798, 2021.

[83] P. Eirich, T. Wech, J. Heidenreich, *et al.*, "Cardiac real-time MRI using a pre-emphasized spiral acquisition based on the gradient system transfer function," *Magnetic Resonance in Medicine*, vol. 85, no. 5, pp. 2747–2760, 2020.

[84] G. Kowalik, D. Knight, J. Steeden, *et al.*, "Perturbed spiral real-time phase-contrast MR with compressive sensing reconstruction for assessment of flow in children," *Magnetic Resonance in Medicine*, vol. 83, no. 6, pp. 2077–2091, 2019.

[85] S. Lingala, B. Sutton, M. Miquel, *et al.*, "Recommendations for real-time speech MRI," *Journal of Magnetic Resonance Imaging*, vol. 43, no. 1, pp. 28–44, 2015.

[86] K. Tha, C. Stehning, Y. Suzuki, *et al.*, "Noninvasive evaluation of electrical conductivity of the normal brain and brain tumors," in *Proceedings of the 22th Annual Meeting of ISMRM*, 1885, Milan, Italy, 2014.

[87] S. Mandija, E. Meliadò, N. Huttinga, *et al.*, "Opening a new window on MR-based electrical properties tomography with deep learning," *Scientific Reports*, vol. 9, no. 1, pp. 1–9, 2019.

[88] S. Gavazzi, C. van den Berg, M. Savenije, *et al.*, "Deep learning-based reconstruction of in vivo pelvis conductivity with a 3D patch-based convolutional neural network trained on simulated MR data," *Magnetic Resonance in Medicine*, vol. 84, no. 5, pp. 2772–2787, 2020.

[89] K. Jung, S. Mandija, J. Kim, *et al.*, "Improving phase-based conductivity reconstruction by means of deep learning–based denoising of B1+ phase data for 3T MRI," *Magnetic Resonance in Medicine*, vol. 86, no. 4, pp. 2084–2094, 2021.

[90] K. Jung, S. Mandija, C. Cui, *et al.*, "Data-driven electrical conductivity brain imaging using 3T MRI," *Human Brain Mapping*, vol. 44, no. 15, pp. 4986–5001, 2023.

Acknowledgement

First and foremost, I would like to express my gratitude to Prof. Frank Zöllner. Especially for providing me with anything I need, from gadolinium bottles to couple thousands worth finite element solver and for letting me explore anything I want during my PhD journey.

I would also thank Prof. Lothar Schad, for his creation of the best MRI community: Computerunterstütze Klinische Medizin. It was an honor to be a part of this group.

I would like to express my gratitude to Dr. Dennis Kleimaier. Visiting your office was a great way to start a day for me. Ever patient, from my almost non-existent German to exhausting hiking trips, or as they call in Bavaria "a quite moderate Sunday walk". With Kristina, I hope your days will be even lovelier than her delicious plum cakes!

It would be very hard to have this thesis without the help of, now officially, Dr. Efe Ilıcak. I will miss being your guinea pig, many times on the verge of any SAR and PNS limits possible. It was also quite fun to have a project together, may your future research ever be as smooth as your DMD paper.

I have to thank the best officemate ever: (soon to be Dr.) Simon Reichert. He had many aspects: My accomplice in failing to take care of one single, simple, poor plant in our office. My protector from invading bugs. My sensei in our gym sessions (though you also need to learn Bulgarian split squad).

CKM was the best MRI community, because it has the best people in the entire MRI community. I would like to thank Steffen, Christian, Patrick, and Dominik, our current members, for their presence in Mittagspause, which held wonderfully intriguing conversations, their best efforts to teach me Tischkicker (and unfortunately failing miserably, but totally not their fault). Additionally, I want to express my gratitude to the former members of CKM: Valerie, Anne, and Jorge. Our glorious Mannheim was even more dazzling with your presence.

Special thanks to my old Bilkent gang, Eren and Mustafa. It is really great to have friends, who saw your worst and did not leave. It will be very nice to see their best, including their, now extending, families!

My beacon of joy, Irène. I am sure, in one of our many future days together, I will be able to pronounce your name correctly. You were the reason for me to stay sane through this journey and I hope I will have a blue ribbon in my brain soon!

Lastly, I owe my gratitude to my parents and my sister (this time I did not forget), who supported me every time I need. I am really lucky to have them (that includes my sister too).

Declaration

This thesis is the result of my independent investigation under supervision. Where my work is indebted to the work or ideas of others, for example from the literature or the internet, I have acknowledged this within the thesis.

I declare that this study has not already been accepted for any degree, nor is it currently being submitted in candidature for any other degree.

I am aware that a false declaration could have legal implications.

Erklärung

Ich versichere, dass ich diese Arbeit selbstständig verfasst habe und keine anderen als die angegebenen Quellen und Hilfsmittel benutzt habe.

Heidelberg, July 15, 2024

Safa Özdemir